Temperature change-induced linear and nonlinear axial responses of internal replacement pipe (IRP) systems for pipeline rehabilitation incorporating the effects of soil friction

Hamid Ahmadi [a,*], Allan Manalo [a], Patrick G. Dixon [b], Ahmad Salah [a], Warna Karunasena [a], Cam Minh Tri Tien [a], Shanika Kiriella [a], Thomas D. O'Rourke [c], Brad P. Wham [b]

[a] *Centre for Future Materials, University of Southern Queensland, Toowoomba, QLD 4350, Australia*
[b] *Center for Infrastructure, Energy, and Space Testing, University of Colorado Boulder, Boulder, CO 80309, USA*
[c] *School of Civil and Environmental Engineering, Cornell University, Ithaca, NY 14853, USA*

ABSTRACT

The internal replacement pipe (IRP) is a developing trenchless system utilised for restoring buried steel and cast-iron legacy pipelines. It is crucial to ensure that this advanced system is appropriately designed to reinstate the functionality of damaged pipelines effectively and safely. The present paper investigates the structural response of IRP systems used in repairing pipelines with circumferential discontinuities subjected to seasonal temperature changes. Analytical and numerical approaches verified via experimental data and available closed-form solutions were implemented to analyse a total of 180 linear and nonlinear finite element (FE) simulations. A set of analytical expressions was developed to describe the loading and induced responses of the system. Based on an extensive FE parametric study, five modification factors were derived and applied to developed analytical expressions to characterise the structural response incorporating the effects of soil friction. Results showed that there is a major difference between the results of linear and nonlinear analyses highlighting the importance of including the material nonlinearities in the FE analysis. A significant difference was observed between the discontinuity openings with and without the consideration of soil friction implying that appropriate inclusion of soil friction in the FE model is crucial to get realistic system responses subjected to temperature change. Although the application of IRP holds immense promise as a trenchless solution for rehabilitating legacy pipelines, the lack of established design procedures and standards for these technologies has restricted their application in gas pipelines. Results obtained from numerical and analytical models developed in the present research will provide valuable insights for the design and development of safe and efficient IRP systems urgently needed in the pipeline industry.

1. Introduction

Pipeline infrastructure plays a vital role in modern society, serving as the lifeline for various sectors and ensuring the smooth functioning of essential services. Pipelines are crucial for the transportation of oil, gas, and other vital fluids, efficiently and reliably over long distances, facilitating energy supply and supporting economic growth. Over time, buried pipelines can sustain damage due to a range of factors including wear and tear [1], corrosion [2–4], and external forces such as ground water pressure [5], earthquakes [6,7], and landslides [8,9]. Pipeline operators frequently undertake inspection and rehabilitation efforts aimed at identifying and resolving such problems proactively, preventing them from escalating into more significant issues [10]. Hence, maintenance and repair are of paramount importance to ensure the integrity and reliability of pipeline infrastructure.

Trenchless methods, which involve the rehabilitation of pipelines without extensive excavation, have garnered significant attention [11, 12]. These methods present numerous advantages compared to traditional excavation-based approaches. They minimize disruption to the environment, particularly in urban or densely populated areas [13], and offer faster completion times and lower overall costs [14–16]. Moreover, they prove valuable in rehabilitating pipelines located in challenging or

(a)

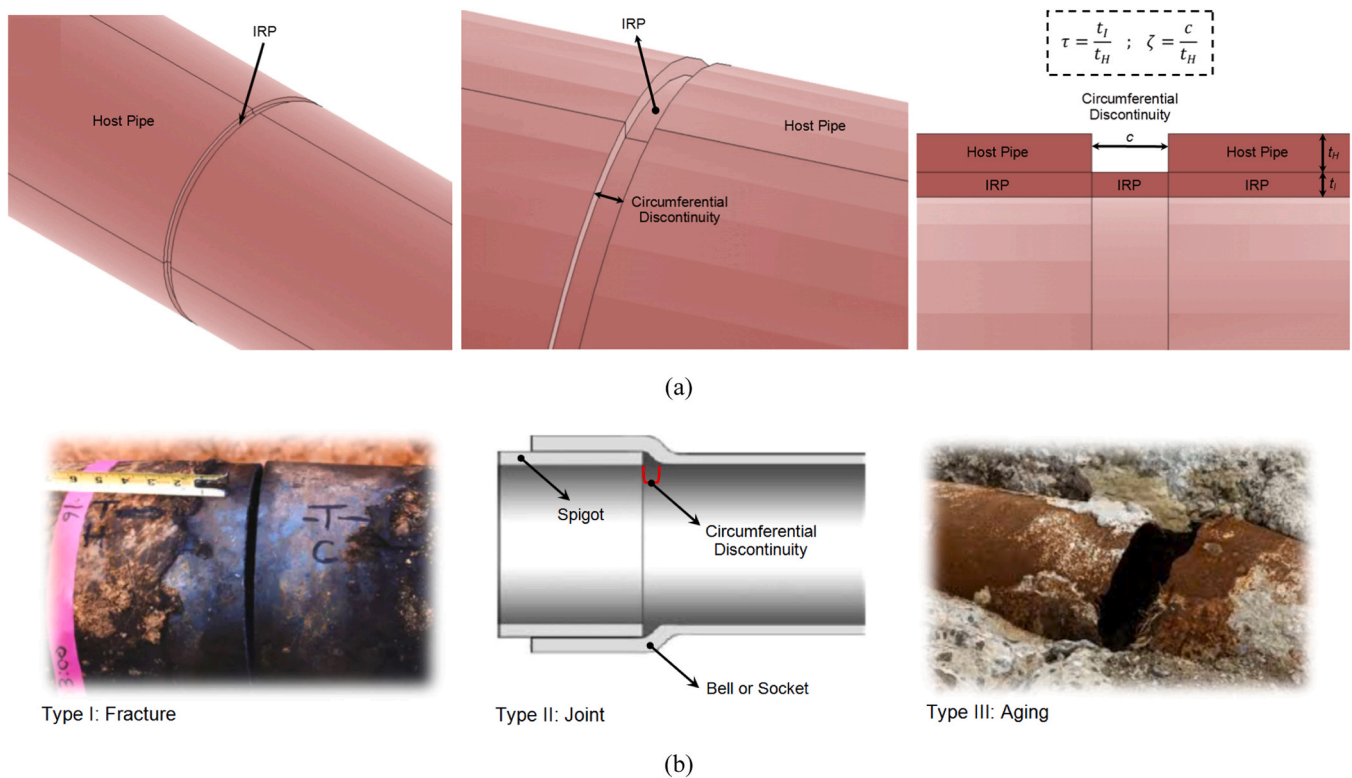Type I: Fracture   Type II: Joint   Type III: Aging

(b)

Fig. 1. (a) Geometrical notation for a host pipe with a circumferential discontinuity rehabilitated with IRP, (b) Three major types of circumferential discontinuity in legacy gas pipelines.

inaccessible areas [17], making them an invaluable resource for pipeline operators and municipalities seeking cost-effective and environmentally sustainable infrastructure maintenance [18,19].

In recent years, trenchless repair technologies have made significant progress, particularly with the development of internal replacement pipe (IRP) systems using metals, polymeric materials, and composites [20,21]. An IRP system, in the context of trenchless rehabilitation, refers to the method of replacing old, worn out or damaged pipes with new pipes or liners. This solution addressing issues such as corrosion, leaks, or structural deficiencies requires little to no excavation and can be usually carried out from the nearest manholes. In this system, a new pipe/liner is inserted into an existing one, or a new pipe is formed inside the old one thorough spraying materials onto the inner surface of the host pipe by a machine which can go into and move along the host pipe.

The use of IRP holds immense promise as a trenchless solution for rehabilitating bare steel and cast-iron legacy gas pipelines. However, the lack of established design procedures and standards for these technologies has restricted their application in gas pipelines. Therefore, it is crucial to conduct a thorough investigation into the structural behaviour of emerging IRP systems under applied loads and to effectively design them as internal repair systems for gas pipeline rehabilitation.

Dixon et al. [22] have identified nine key performance objectives crucial for the efficient design of legacy gas pipelines utilizing pipe-in-pipe (PIP) rehabilitation technologies: cyclic in-service surface loads [23,24], lateral deformation, puncture/impact [25], ovalisation [26], axial deformation [27], hoop stress [28], compatibility with current and future fluid compositions [29], debonding at PIP-host pipe interface [30], and service connections [31]. According to this state-of-the-art review, one of the potential failure modes observed in pipelines and internal replacement pipe (IRP) systems is associated with excessive thermal strains and the resulting stresses. For instance, in 2006, BP had to halt operations on segments of its Prudhoe Bay Pipeline in Alaska due to severe damage resulting from excessive thermal strains, leading to cracks and leaks [32]. Similarly, in 2021, the Colonial

Pipeline experienced a mechanical failure caused by thermal expansion and contraction after being shut down due to a cyber-attack. This subsequent failure resulted in fuel shortages and price spikes in multiple states once the pipeline was restarted [33]. Despite the critical importance of safeguarding against thermal load-induced failure through sound design practices, research in this field remains scarce, with no comprehensive study currently available in the literature addressing the structural challenges and design requirements specific to IRP systems under thermal actions.

Jeon et al. [34] and Stewart et al. [35] developed a set of closed-form solutions for the calculation of the crack opening in a cast iron pipe rehabilitated with an internal pipe repair system subjected to a negative temperature change. Although the developed analytical expressions are useful for simplified conservative calculations, they have a number of limitations if a more realistic representation of the system is of interest. These expressions do not include the effects of the internal pipe's stiffness, internal pressure of the pipeline, thermal expansion/contraction of the internal repair pipe, and material nonlinearities on the crack opening and axial response of the system.

An analytical approach was implemented by Dixon et al. [36] to estimate potential levels of axial deformation. Their assessment focuses on movement at a discontinuity, representative of a weak joint or circumferential crack in the host pipe, which is spanned by a rehabilitation internal pipe. Closed-form equations have been derived for induced force and crack opening displacement. Developed expressions include the effects of the soil friction as well as the internal pipe's stiffness and thermal expansion/contraction, but do not consider the role of the internal pressure of the pipeline, material nonlinearities, stress concentrations, and differential displacements along the thickness of IRP and host pipe.

A comprehensive mathematical model has been developed by Bokaian [37] for the thermal expansion of pipe-in-pipe and bundle systems used in offshore oil and gas industry. The aim was to calculate the displacement and forces on the bulkheads and axial force in the inner
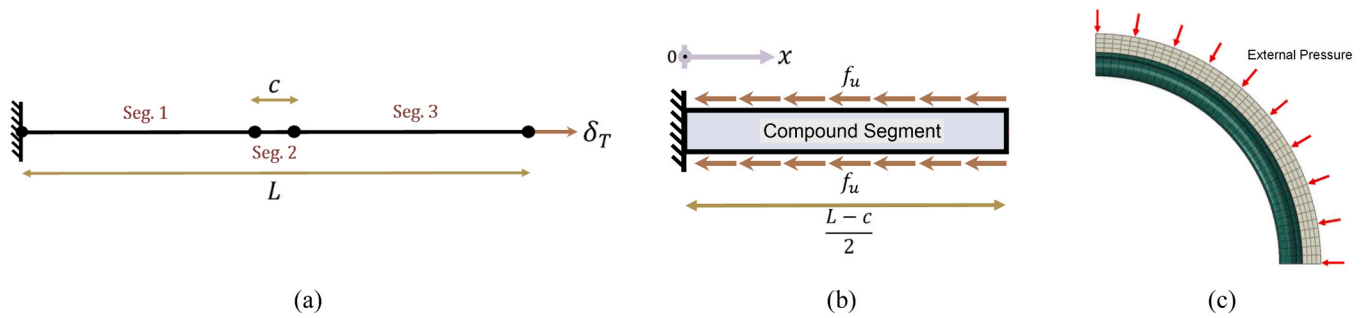
Fig. 2. (a) Schematic representation of an IRP repair system with a host-pipe discontinuity subjected to axial displacement, (b) Compound segment of the mechanical model subjected to soil friction, (c) External pressure on the outer surface of the host pip.e.
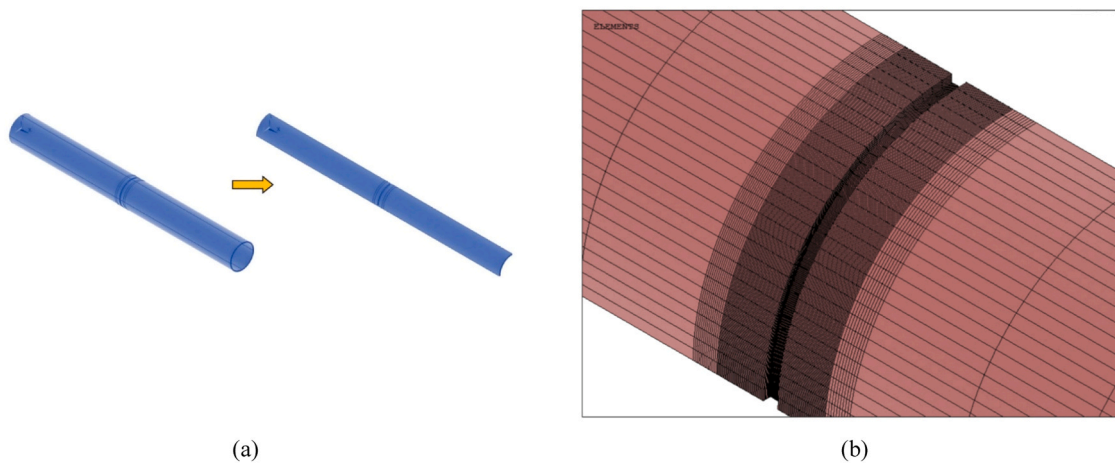

Fig. 3. (a) One fourth of the entire pipe required to be modelled, (b) Generated mesh based on the sub-zone scheme.
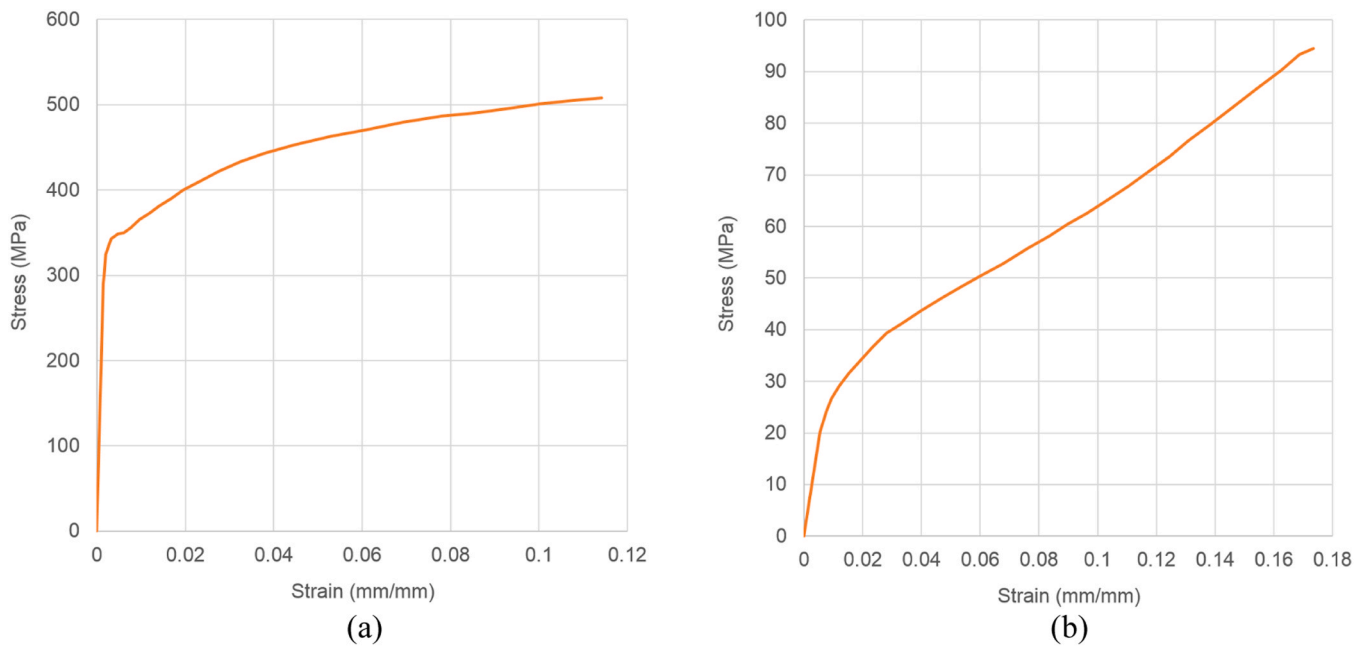
Fig. 4. True stress-strain curves used for the FE analysis: (a) API 5L X42 steel, (b) ALTRA10®.

pipe. No discontinuity along the pipeline was assumed in this study which creates limitations for its application to gas distribution pipelines. A set of finite element (FE) stress analyses was carried out by Lu et al. [38] on urban gas pipeline repaired by inserted hose lining method.

However, their study does not cover the effects of temperature changes and host pipe discontinuities on the structural response of the system. Failure modes of PIP repair systems for water and gas pipelines were analysed by Tafsirojjaman et al. [25]. The focus of their research work

$$\phi_U = \frac{\delta_{1U} - \delta_{2U}}{\mu \delta_T}$$

$$\phi_M = \frac{\delta_{1M} - \delta_{2M}}{\mu \delta_T}$$

$$\phi_L = \frac{\delta_{1L} - \delta_{2L}}{\mu \delta_T}$$

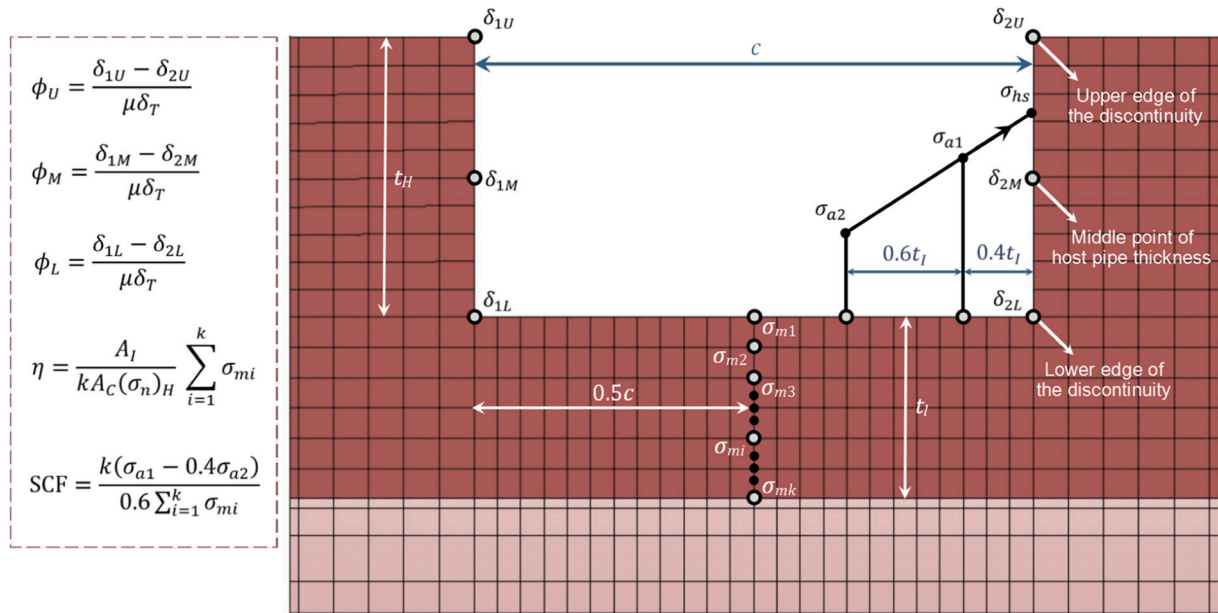$$\eta = \frac{A_I}{k A_C (\sigma_n)_H} \sum_{i=1}^{k} \sigma_{mi}$$

$$\text{SCF} = \frac{k(\sigma_{a1} - 0.4\sigma_{a2})}{0.6 \sum_{i=1}^{k} \sigma_{mi}}$$

Fig. 5. Extraction of parameters ϕ_U, ϕ_M, ϕ_L, η, and SCF from the FE model.
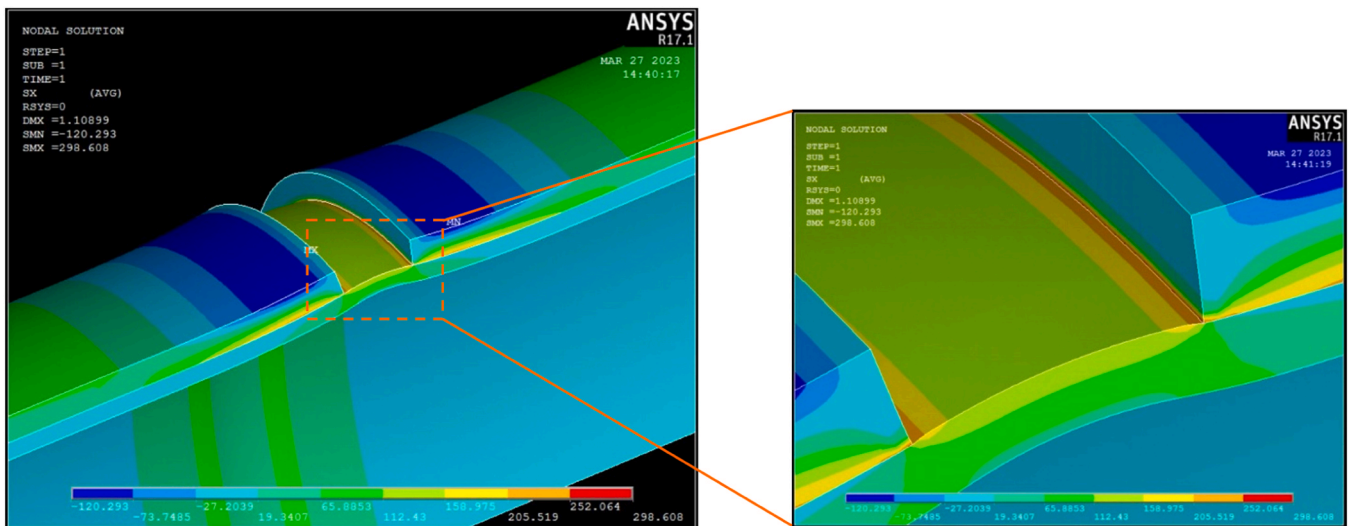

Fig. 6. Deformed shape of IRP system subjected to axial displacement (contours: axial stress [MPa]).

was the behaviour of the repair pipe alone; and the effects of host pipe properties, possible circumferential discontinuities, and material non-linearities were not considered in the thermal analysis.

The preceding discussion highlights that the axial structural responses of internal replacement pipe (IRP) systems under temperature changes, particularly in scenarios involving pipeline discontinuities (Fig. 1a), have not been extensively studied. Three primary types of circumferential discontinuity can be observed in host pipes (Fig. 1b): Type I, characterized by circumferential fracture resulting from weld failure, impact, or fatigue-induced progressive crack propagation; Type II, involving circumferential discontinuity at bell and spigot joints; and Type III, which entails circumferential discontinuity due to the removal of a significant portion of the host pipe due to aging. In all these instances, it is crucial to make sure that the IRP is appropriately designed to ensure satisfactory performance during service.

This paper presents an analytical and numerical investigation on the structural response of an IRP system utilized in rehabilitating pipelines with a circumferential discontinuity under varying seasonal temperature conditions. The study consists of four major phases to achieve the research objective. In Phase I, a mechanical model was developed for the IRP system with a host-pipe circumferential discontinuity incorporating the frictional effects of surrounding soil, and analytical expressions were derived to describe the loading and induced responses to seasonal temperature changes. Phase II involved parametric stress analyses on 180 finite element (FE) models of IRP repair systems subjected to axial displacement. These FE models were validated using experimental data and closed-form solutions. Effects of geometrical parameters and material characteristics of the system as well as the pipeline's internal pressure, burial depth of the pipe, and properties of the surrounding soil on axial stresses and displacements due to seasonal temperature variations were investigated. Phase III focused on deriving modification factors based on the FE results, which can be applied to the analytical expressions to estimate the IRP's peak axial stress and opening of the host-pipe circumferential discontinuity caused by temperature changes. These modification factors consider stress concentration at the discontinuity edge, stress distribution along

Table 1
Characteristics of LS03 FE model used for the verification of numerical results.

Parameter	Symbol	Unit	Value (s)
Temperature change [35,53]	ΔT	°C	27.8
MoE of IRP [45]	E_I	MPa	3769.2
Poisson's ratio of IRP [45]	ν_I	-	0.23
CTE of IRP [47]	α_I	1/°C	45×10^{-6}
MoE of the host pipe [43]	E_H	MPa	210700
Poisson's ratio of the host pipe [43]	ν_H	-	0.3
CTE of the host pipe [44]	α_H	1/°C	12×10^{-6}
Discontinuity width	c	mm	12.7
Wall thickness of IRP [54]	t_I	mm	4.115
Cross sectional area of IRP	A_I	mm^2	3969.24
Outer diameter of the host pipe [54]	D_{oH}	mm	323.85
Wall thickness of the host pipe [54]	t_H	mm	6.35
Cross sectional area of the host pipe	A_H	mm^2	6330.4
Inner diameter of the host pipe	D_{iH}	mm	311.15
Friction angle at the soil/host pipe interface	ψ	°	31
Coefficient of lateral earth pressure at rest [35]	K_0	-	1
Effective unit weight of the soil [35]	γ'	N/mm^3	19.6×10^{-6}
Burial depth to the pipe's centreline	z	mm	1100
Pipe displacement required to mobilize full soil resistance [35]	δ_u	mm	1
Internal pressure of the pipeline [54]	p_i	MPa	0.45

Table 2
Results of the FE verification process based on analytical predictions.

Parameter	FE result	Analytical prediction	Difference
Nominal axial stress of IRP, $(\sigma_n)_I$	42.735 MPa	43.235 MPa	1.2%
Nominal value of discontinuity opening, $(\delta_c)_n$	0.140 mm	0.146 mm	4.1%

Table 3
Results of the FE model verification against closed-form solutions.

Parameter	Closed-form solution	FE result	Difference
Hoop stress, σ_θ	24.5 MPa	24.528 MPa	0.1%
Longitudinal stress, σ_l	7.35 MPa	7.083 MPa	3.7%
Radial stress, σ_r	-1 MPa	-0.918 MPa	8.2%
Total axial deformation, δ_T	0.103 mm	0.106 mm	2.8%

the IRP thickness, and differential displacements along the thickness of IRP and host pipe. Lastly, Phase IV involved a study on the effects of material and geometric nonlinearities on the axial response under seasonal temperature variations considering the effects of soil friction. Results obtained from the developed numerical and analytical models will provide valuable insights for the design and development of safe and efficient IRP repair systems urgently needed in the pipeline industry.

Table 4
Geometrical and material properties of S01 and S02 specimens prepared for the experimental tests.

Parameter	Value
MoE of ALTRA10® IRP	3769.2 MPa
Poisson's ratio of ALTRA10® IRP	0.23
Wall thickness of ALTRA10® IRP	4.115 mm
Young's modulus of steel host pipe	210700 MPa
Poisson's ratio of steel host pipe	0.3
Wall thickness of steel host pipe	6.35 mm
Outer diameter of steel host pipe	323.85 mm
Discontinuity width	12.7 mm (S01), 152.4 mm (S02)
Pipe length	3048 mm

2. Methodology

2.1. Formulation of the discontinuity opening as a function of temperature change

2.1.1. Analytical expression of applied axial displacement to simulate the thermal effects

A compound section of host pipe and IRP is considered with a circumferential host-pipe discontinuity at the midspan of the pipe. The entire length of the pipe consists of three segments: a 'discontinuity' segment (Seg. 2) which only includes the IRP section and two 'compound' segments (Segs. 1 and 3) at the two sides of the discontinuity segment. At the compound segments, both IRP and host pipe sections are present (Fig. 2a). In a compound section, even if the axial deformation is unconstrained, a uniform temperature change can still induce axial stresses in the pipe. The reason is that the values of the coefficient of thermal expansion (CTE), as a material property, are different for IRP and host pipe. The variable of interest, derived in this section, is the axial displacement that should be applied to the free end of the pipe in the mechanical model of Fig. 2a to simulate the axial deformation of the system subjected to the temperature change considering the friction between the host pipe's outer surface and surrounding soil.

If IRP and host pipe are fully bonded, total axial deformation of the system (δ_T) due to the temperature change, assuming linear material behaviour, can be calculated as follows.

$$\delta_T = \delta_t + \delta_f = \sum_{i=1}^{3} \delta_{it} + \sum_{i=1}^{3} \delta_{if} \tag{1}$$

where δ_{it} and δ_{if} are the axial deformations of the ith segment due to the temperature change ΔT and soil friction, respectively.

Following expressions describe the δ_{it} for Segs. 1, 2, and 3.

$$\delta_{1t} = \delta_{3t} = \alpha_C \left(\frac{L-c}{2} \right) \Delta T \quad ; \quad \delta_{2t} = \alpha_I c \Delta T \tag{2}$$

where L is the total length of the pipe; c is the discontinuity width; α_I is the CTE of IRP; and α_C is the equivalent CTE of the compound section.

Closed-form solution for δ_{if} is as follows (Fig. 2b).

$$\delta_{1f} = \delta_{3f} = \delta(x)|_{x=\frac{L-c}{2}} \quad ; \quad \delta_{2f} = 0 \tag{3}$$

where $\delta(x)$ is axial displacement along the pipe which can be obtained by Eq. (4).

$$\delta(x) = \int_0^x \varepsilon(x)dx = \int_0^x \frac{F(x)}{E_C A_C} dx \tag{4}$$

where $\varepsilon(x)$ is the axial strain, $F(x)$ is the axial internal force, A_C is the area of the compound cross section of host pipe and IRP, and E_C is the elastic modulus of the compound segment.

It should be noted that the exact value of δ_{2f} is nonzero. However, due to the short length of the discontinuity segment compared to the entire pipe length ($c \ll L$) and considering the fact that the full contact between the soil and the exposed IRP in the discontinuity segment is unlikely, the value of δ_{2f} can be reasonably assumed to be zero.

Axial internal force along the pipe is calculated as follows (Fig. 2b).

$$F(x) = \int_x^{\frac{L-c}{2}} (-f_u)dx = -f_u \left(\frac{L-c}{2} \right) + f_u x \tag{5}$$

where f_u is the soil friction force per unit length of the pipe, which is assumed to be constant over the entire pipe length.

Substitution of Eq. (5) into Eqs. (3 and 4) results in the following expression for δ_{1f}.
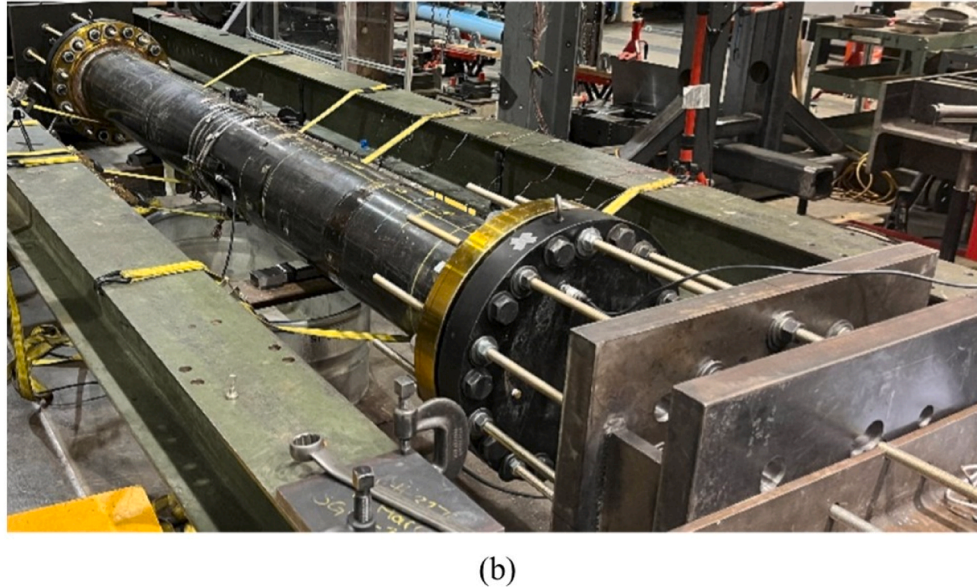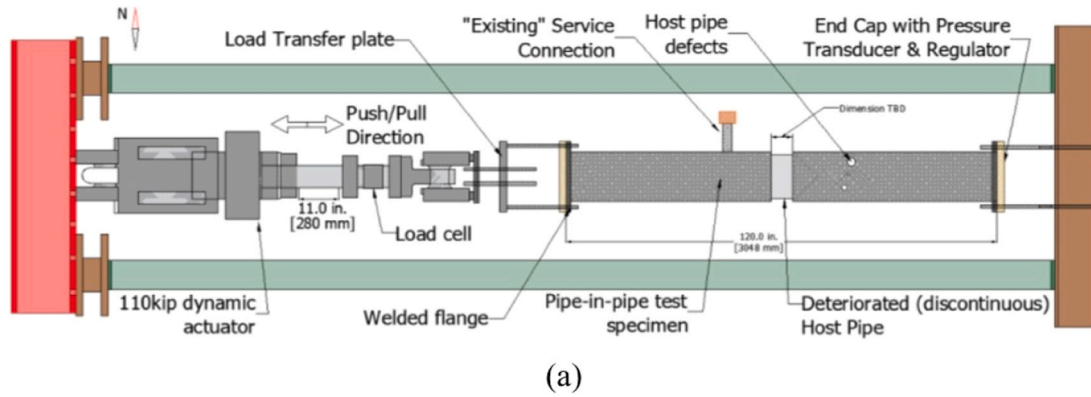
Fig. 7. Experimental tests conducted at the University of Colorado Boulder: (a) Setup for axial pull-push tests, (b) S01 specimen.

Table 5
Results of the FE model verification using experimental data.

Parameter	Specimen	Debonded length	Experimental value	FE result	Difference
Discontinuity opening	S01	95 mm	0.73 mm	0.77 mm	5.5%
	S02	150 mm	2.95 mm	3.04 mm	3.1%

$$\delta_{1f} = \int_0^{\frac{L-c}{2}} \left[\frac{-f_u\left(\frac{L-c}{2}\right) + f_u x}{E_C A_C} \right] dx = -\frac{f_u(L-c)^2}{8E_C A_C} \qquad (6)$$

Substitution of Eqs. (2), (3), and (6) into Eq. (1) leads to the following analytical expression for δ_T.

$$\delta_T = \alpha_C(L-c)\Delta T + \alpha_I c \Delta T - \frac{f_u(L-c)^2}{4E_C A_C} \qquad (7)$$

In Eq. (7), the equivalent CTE of the compound section, α_C, can be expressed by Eq. (8) (see Appendix 1 for the derivation).

$$\alpha_C = \frac{E_I A_I \alpha_I + E_H A_H \alpha_H}{E_I A_I + E_H A_H} \qquad (8)$$

where α_I and α_H are the CTE of IRP and host pipe, respectively; E_I and E_H are the modulus of elasticity (MoE) for IRP and host pipe, respectively; and A_I and A_H are cross sectional area of IRP and host pipe, respectively.

The term $E_C A_C$ in Eq. (7), can be expressed in terms of material and geometrical properties of IRP and host pipe as shown in Eq. (9) (see Appendix 1 for the derivation).

$$E_C A_C = E_I A_I + E_H A_H \qquad (9)$$

Based on Eqs. (8) and (9), Eq. (7) can be rewritten as follows.

$$\delta_T = \Delta T \left[\alpha_I c + \frac{E_I A_I \alpha_I + E_H A_H \alpha_H}{E_I A_I + E_H A_H}(L-c) \right] - \frac{f_u(L-c)^2}{4(E_I A_I + E_H A_H)} \qquad (10)$$

Soil friction force per unit length of the pipe (f_u) can be formulated as follows.

$$f_u = 4\mu_k N \qquad (11)$$

where μ_k is the coefficient of friction between the soil and the outer surface of the host pipe, and N is the normal force per unit length of the pipe acting on the outer surface of the host pipe's quarter section due to the application of soil pressure (Fig. 2c) which can be expressed as Eq. (12).

Table 6

Values of input parameters for 132 sets of analytical calculations and 72 linear and nonlinear FE analyses to study the effects of pipeline's internal pressure/burial depth, soil properties, and material/geometric nonlinearities on axial responses of IRP system.

Parameter	Symbol	Unit	Value (s)
Soil/host pipe interface friction angle [56]	ψ	°	21, 26, 31, 36, 41, 46
Effective unit weight of the soil	γ'	N/mm^3	12×10^{-6}, 14×10^{-6}, 16×10^{-6}, 18×10^{-6}, 20×10^{-6}, 22×10^{-6}
Burial depth of the pipe	z	mm	1100, 1350, 1600, 1850, 2100, 2350
Coefficient of lateral earth pressure	K_0	-	0.4, 0.5, 0.6, 0.7, 0.8, 0.9
Pipe displacement to mobilize full soil resistance	δ_u	mm	0.25, 0.5, 1, 2, 4
Temperature change [35, 53,55]	ΔT	°C	27.8, 55.0
Pipeline's internal pressure [22,54]	p_i	MPa	0, 0.25, 0.5, 0.75, 1
MoE of the host pipe [43]	E_H	MPa	210700
Poisson's ratio of the host pipe [43]	ν_H	-	0.3
CTE of the host pipe [44]	α_H	1/°C	12×10^{-6}
MoE of IRP [45]	E_I	MPa	3769.2
Poisson's ratio of IRP [45]	ν_I	-	0.23
CTE of IRP [47]	α_I	1/°C	45×10^{-6}
Discontinuity width [54]	c	mm	12.7
Outer diameter of the host pipe [54]	D_{oH}	mm	323.85
Wall thickness of the host pipe [54]	t_H	mm	6.35
Inner diameter of the host pipe	D_{iH}	mm	311.15
Cross sectional area of the host pipe	A_H	mm^2	6330.4
Wall thickness of IRP [54]	t_I	mm	4.115
Cross sectional area of IRP	A_I	mm^2	3969.24

Table 7

Values of input parameters for 108 FE models analysed to characterise parameters ϕ_U, ϕ_M, ϕ_L, η, and SCF.

Parameter	Symbol	Unit	Value (s)
MoE of IRP	E_I	MPa	1000, 3769.2, 10,000, 15,000, 24,500, 69,000
Wall thickness of IRP	t_I	mm	2.54, 4.115, 5.715, 7.3025, 8.89, 10.4775
Discontinuity width	c	mm	6.35, 12.7, 152.4
t_I/t_H ratio	τ	-	0.4, 0.65, 0.9, 1.15, 1.4, 1.65
c/t_H ratio	ζ	-	1, 2, 24
MoE of the host pipe [43]	E_H	MPa	210700
Poisson's ratio of the host pipe [43]	ν_H	-	0.3
CTE of the host pipe [44]	α_H	1/°C	12×10^{-6}
Poisson's ratio of IRP [45]	ν_I	-	0.23
CTE of IRP [47]	α_I	1/°C	45×10^{-6}
Outer diameter of the host pipe [54]	D_{oH}	mm	323.85
Wall thickness of the host pipe [54]	t_H	mm	6.35
Friction angle at the soil/host pipe interface [35]	ψ	°	32
Effective unit weight of the soil [35]	γ'	N/mm^3	19.6×10^{-6}
Burial depth of the pipe [35]	z	mm	1080
Coefficient of lateral earth pressure [35]	K_0	-	1
Pipe displacement to mobilise full soil resistance [35]	δ_u	mm	1
Temperature change [35,53]	ΔT	°C	27.8
Internal pressure of the pipeline [54]	p_i	MPa	0.45
Maximum mobilized soil friction force/length (Eq. (14))	f_u	N/mm	13.46
Total length of the pipe (Eq. (20)—(23))	L	mm	86,469.06

$$N = \int_0^{\pi/2} p_o r_{oH} d\theta = 0.25 p_o \pi D_{oH} \tag{12}$$

where D_{oH} is the outer diameter of the host pipe, and p_o is the applied soil pressure.

Applied soil pressure to be used in Eq. (12) can be assumed as the average of vertical and horizontal stresses in the soil due to its weight ($\sigma_v = \gamma' z$; $\sigma_h = K_0 \gamma' z$) [39]. Hence, values of the soil pressure on the host pipe and the friction coefficient can be obtained as follows.

$$p_o = \left(\frac{1+K_0}{2}\right)\gamma' z \quad ; \quad \mu_k = \tan\psi \tag{13}$$

where γ' is the effective unit weight of the soil, z is the burial depth to the pipe's centreline, K_0 is the coefficient of lateral earth pressure at rest, and ψ is the friction angle at the interface between the soil and the host pipe. With the substitution of Eq. (13) into Eqs. (11) and (12), soil friction force per unit length of the pipe can be formulated as Eq. (14).

$$f_u = \left(\frac{1+K_0}{2}\right)\gamma' z \tan\psi \pi D_{oH} \tag{14}$$

Based on Eq. (14), Eq. (10) can be rewritten as follows.

$$\delta_T = \Delta T \left[\alpha_I c + \frac{E_I A_I \alpha_I + E_H A_H \alpha_H}{E_I A_I + E_H A_H}(L-c)\right] - \frac{(1+K_0)\gamma' z \tan\psi \pi D_{oH}}{8(E_I A_I + E_H A_H)}(L-c)^2 \tag{15}$$

2.1.2. Nominal value of the discontinuity opening

Nominal value of the discontinuity opening, $(\delta_c)_n$, can be expressed

as a function of the applied axial displacement (δ_T in Eq. (15)) as follows.

$$(\delta_c)_n = \mu(c, L, E_I, A_I, E_H, A_H)\cdot\delta_T \tag{16}$$

where μ is a transfer function which can be expressed in terms of the geometrical and material properties of the system as follows (see Appendix 2 for the derivation).

$$\mu = \frac{c}{E_I A_I \left(\frac{c}{E_I A_I} + \frac{L-c}{E_H A_H + E_I A_I}\right)} \tag{17}$$

2.1.3. Actual discontinuity opening

Actual values of the discontinuity opening, δ_c, were obtained from a set of linear stress analyses conducted on 108 FE models with different geometrical and material characteristics. Three FE-driven parameters were then defined (ϕ_U, ϕ_M, and ϕ_L) to transform the values of nominal discontinuity opening, $(\delta_c)_n$, to the δ_c values as follows.

$$(\delta_c)_U = \phi_U \cdot (\delta_c)_n$$

$$(\delta_c)_M = \phi_M \cdot (\delta_c)_n$$

$$(\delta_c)_L = \phi_L \cdot (\delta_c)_n \tag{18}$$

where $(\delta_c)_U$, $(\delta_c)_M$, and $(\delta_c)_L$ are values of actual discontinuity opening obtained from the FE analysis based on the axial displacements of upper, middle, and lower points of the host pipe thickness, respectively.

2.1.4. General expression to describe the opening of a circumferential discontinuity

The combination of Eqs. (15) and (16)—(18) leads to the following expression for the opening of a circumferential host-pipe discontinuity
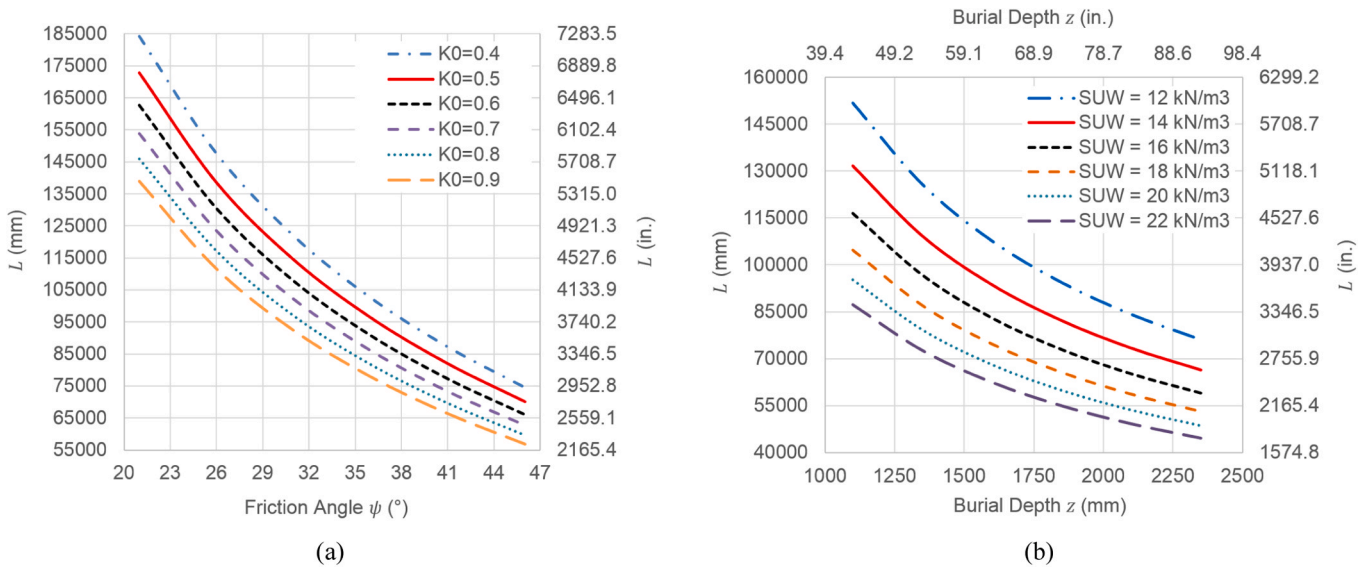
Fig. 8. Variations of the adequate pipe length (L) for mechanical model with (a) coefficient of lateral earth pressure at rest and the friction angle between the soil and the host pipe, (b) pipe burial depth and effective unit weight of the soil.
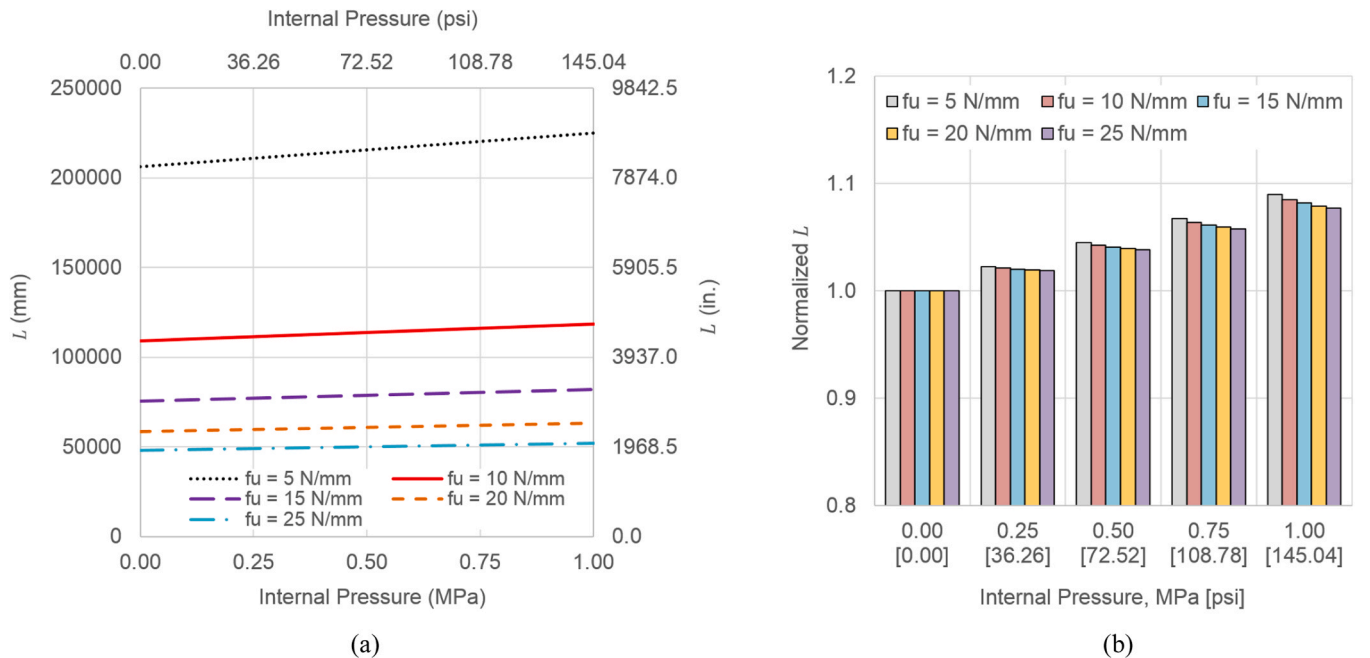

Fig. 9. (a) Effects of the internal pressure and f_u on the value of the pipe length in an equivalent mechanical model, (b) The ratio of pipe length in a mechanical model with an arbitrary internal pressure to the pipe length in the corresponding model with zero internal pressure.

in an IRP system due to the temperature change.

$$
\begin{bmatrix} (\delta_c)_U \\ (\delta_c)_M \\ (\delta_c)_L \end{bmatrix} = \frac{c}{E_I A_I \left(\frac{c}{E_I A_I} + \frac{L-c}{E_H A_H + E_I A_I} \right)}
$$

$$
\cdot \left\{ \Delta T \left[\alpha_I c + \frac{E_I A_I \alpha_I + E_H A_H \alpha_H}{E_I A_I + E_H A_H} (L-c) \right] \right.
$$

$$
\left. - \frac{(1 + K_0) \gamma' z \tan\psi \pi D_{oH}}{8(E_I A_I + E_H A_H)} (L-c)^2 \right\} \cdot \begin{bmatrix} \phi_U \\ \phi_M \\ \phi_L \end{bmatrix} \qquad (19)
$$

where values of parameters ϕ_U, ϕ_M, and ϕ_L are specified based on the results of linearly elastic stress analyses conducted on 108 FE models with different geometrical and material properties.

2.1.5. Length of the pipe in the mechanical model considering the soil friction

The pipe in the mechanical model of Fig. 2a should be long enough to generate adequate soil friction to neutralize the force induced by the temperature change, so the displacement at the pipe end can reliably be assumed to be zero. Such pipe length (L) can be approximated using the equations proposed by Stewart et al. [35]. However, the effect of pipeline's internal pressure has not been considered in these equations. In the present paper, Stewart et al. [35] equations have been revised as follows to incorporate the effect of internal pressure in the calculation of the parameter L. For the derivation, the reader is referred to Appendix 3.
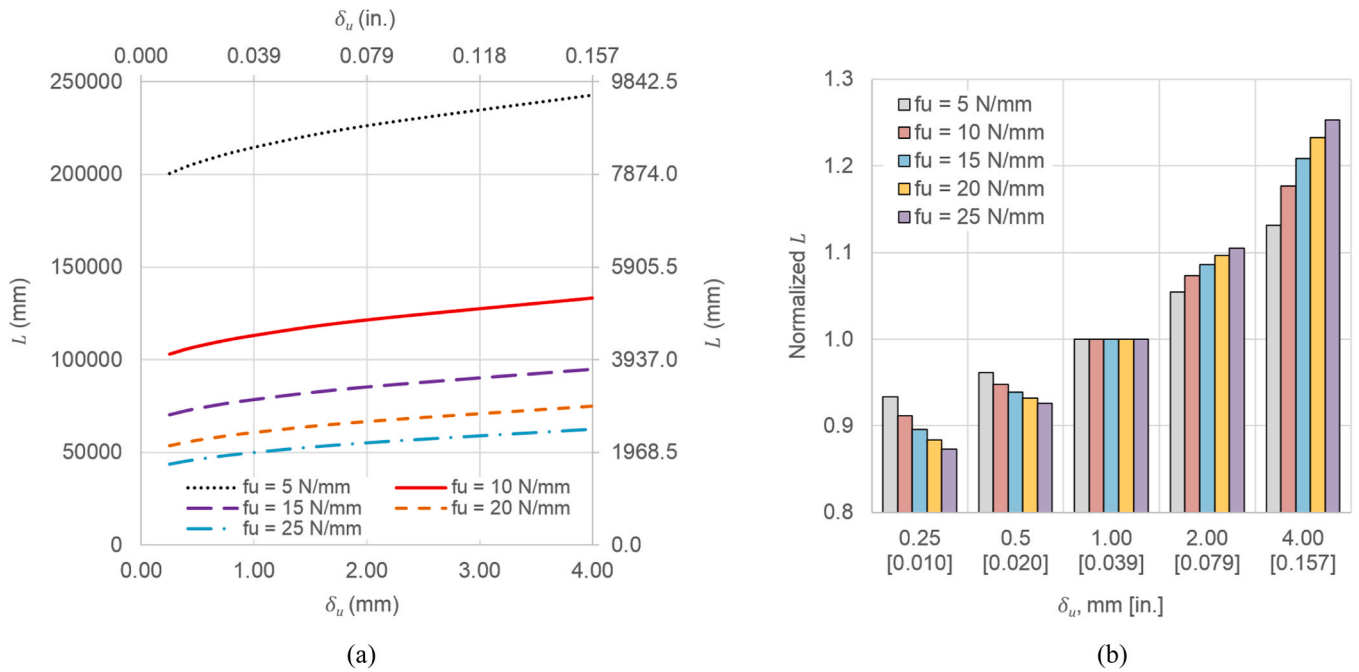
Fig. 10. (a) Effects of δ_u and f_u on the pipe length in an equivalent mechanical model, (b) The ratio of pipe length in a mechanical model with an arbitrary value of δ_u to the pipe length in the corresponding model with $\delta_u = 1$ mm (0.039 in.).
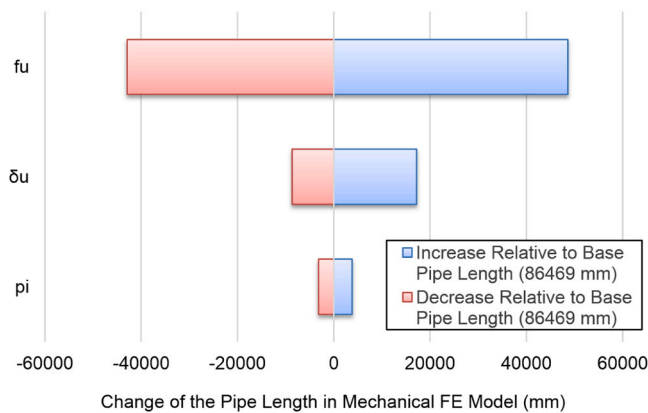

Fig. 11. Effects of parameters p_i, δ_u, and f_u on the required pipe length for a mechanical FE model.

Table 8
Base values for parameters p_i, δ_u, and f_u and the fixed values for all the other parameters required for the calculation of L using Eq. (20)—(23).

Parameter	Symbol	Unit	Value
Inner diameter of the host pipe [54]	D_{iH}	mm	311.15
CTE of the host pipe [44]	α_H	1/°C	12×10^{-6}
MoE of the host pipe [43]	E_H	MPa	210700
Poisson's ratio of the host pipe [43]	ν_H	-	0.3
Wall thickness of the host pipe [54]	t_H	mm	6.35
Cross sectional area of the host pipe	A_H	mm²	6330.4
Internal pressure of the pipeline [54]	p_i	MPa	0.45
Pipe displacement required to mobilize full soil resistance [35]	δ_u	mm	1
Maximum mobilized soil friction force per unit length (Eq. (14))	f_u	N/mm	13.46
Temperature change [35,53]	ΔT	°C	27.8

$$\Delta T^* = \frac{1}{2\alpha_H} \left(\sqrt{\frac{3\delta_u f_u}{E_H A_H}} - \frac{\nu_H p_i D_{iH}}{E_H t_H} \right) \tag{20}$$

$$\acute{l} = \left(\alpha_H \Delta T^* + \frac{\nu_H p_i D_{iH}}{E_H t_H} \right) \frac{2 E_H A_H}{f_u} \tag{21}$$

$$l = \frac{\alpha_H |\Delta T| E_H A_H}{f_u} + \frac{\nu_H p_i D_{iH} A_H}{2 f_u t_H} + \frac{\acute{l}}{2} \tag{22}$$

$$L = 2l \tag{23}$$

In Eq. (20)—(23), p_i is the pipeline's internal pressure, D_{iH} is the inner diameter of the host pipe, t_H is the wall thickness of the host pipe; ν_H is the Poisson's ratio of the host pipe; f_u is the maximum mobilized soil friction force per unit length which can be calculated from Eq. (14); ΔT^* is the amount of the temperature change that is required to mobilize the full soil resistance f_u; δ_u is the amount of the pipe displacement required to mobilize the full soil resistance; $\acute{l}$ is the amount of the pipe length that is required to mobilize the full soil resistance; and L is the amount of the pipe length that will generate enough friction to neutralize the force induced by the temperature change. For $p_i = 0$, Eq. (20)—(23) reduce to the equations previously proposed by Stewart et al. [35].

It is worth mentioning here that according to Stewart et al. [35], the soil friction builds up from zero to f_u over the length $\acute{l}$ from each end of the pipe and then remains constant over the rest of the pipe length. In the present research, such friction build-up has been taken into account through specifying an appropriate pipe length based on Eq. (20)—(23).

2.2. Formulation of IRP's peak axial stress in the discontinuity segment as a function of temperature change

2.2.1. Axial stress in the compound segments of the mechanical model

The internal axial force (F_a) generated in the compound segments due to the application of δ_T (Eq. (15)) to the free end of the pipe can be calculated as follows.
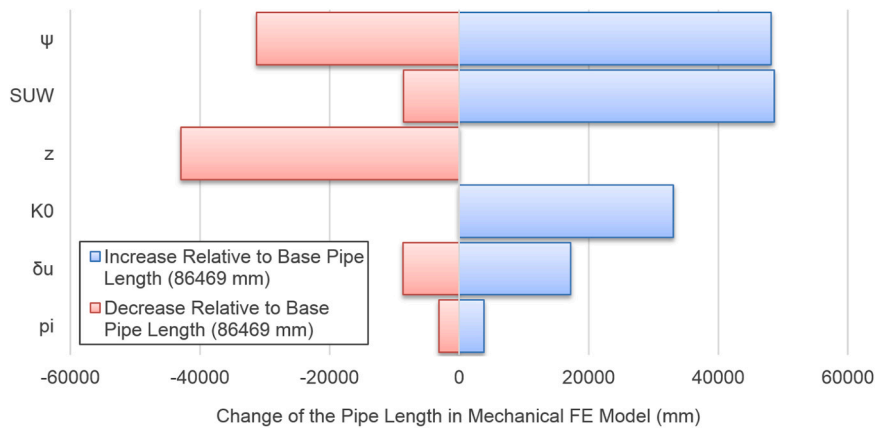
Fig. 12. Effects of parameters K_0, γ', z, ψ, p_i, and δ_u on the pipe length in a mechanical FE model.

Table 9
Base values for parameters K_0, γ', z, and ψ and the fixed value for the remaining parameter (D_{oH}) required for the calculation of f_u using Eq. (14).

Parameter	Symbol	Unit	Value
Coefficient of lateral earth pressure at rest [35]	K_0	-	1
Effective unit weight of the soil [35]	γ'	N/mm^3	19.6×10^{-6}
Burial depth to the pipe's centreline [35]	z	mm	1080
Friction angle at the soil/host pipe interface [35]	ψ	°	32
Outer diameter of the host pipe [55]	D_{oH}	mm	323.85

$$F_a = \delta_T k_T = \frac{\delta_T}{\frac{1}{k_T}} \quad \text{(a)} \quad ; \quad \frac{1}{k_T} = \sum_{i=1}^{3}\frac{1}{k_i} = \frac{\left(\frac{L-c}{2}\right)}{E_C A_C} + \frac{c}{E_I A_I} + \frac{\left(\frac{L-c}{2}\right)}{E_C A_C}$$
$$= \frac{L-c}{E_C A_C} + \frac{c}{E_I A_I} \quad \text{(b)} \tag{24}$$

With the substitution of $E_C A_C$ from Eq. (9), Eq. (24b) is rewritten as follows.

$$\frac{1}{k_T} = \frac{L-c}{E_I A_I + E_H A_H} + \frac{c}{E_I A_I} \tag{25}$$

Substitution of Eqs. (15) and (25) into Eq. (24a) leads to the following expression for the internal axial force:

$$F_a = \frac{\Delta T \left[\alpha_I c + \frac{E_I A_I \alpha_I + E_H A_H \alpha_H}{E_I A_I + E_H A_H}(L-c)\right] - \frac{(1+K_0)\gamma' z \tan\psi \pi D_{oH}}{8(E_I A_I + E_H A_H)}(L-c)^2}{\frac{L-c}{E_I A_I + E_H A_H} + \frac{c}{E_I A_I}} \tag{26}$$

According to Eq. (26), the axial stress of the compound section can be calculated as follows.

$$(\sigma_n)_H = \frac{F_a}{A_C} = \frac{\Delta T \left[\alpha_I c + \frac{E_I A_I \alpha_I + E_H A_H \alpha_H}{E_I A_I + E_H A_H}(L-c)\right] - \frac{(1+K_0)\gamma' z \tan\psi \pi D_{oH}}{8(E_I A_I + E_H A_H)}(L-c)^2}{\left[\frac{L-c}{E_I A_I + E_H A_H} + \frac{c}{E_I A_I}\right](A_I + A_H)} \tag{27}$$
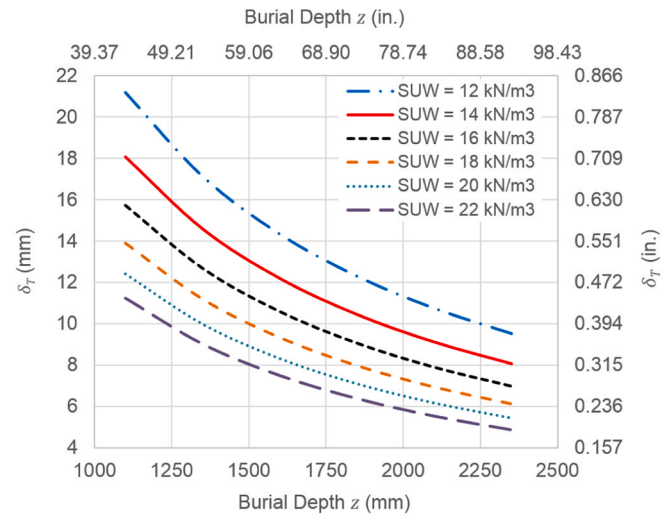
2.2.2. Nominal axial stress of IRP

Nominal axial stress of IRP in the discontinuity segment, $(\sigma_n)_I$, can be expressed as a function of the axial stress of the compound section, wall thicknesses of IRP (t_I) and host pipe (t_H), and outer diameter of the host pipe (D_{oH}) as depicted in Eq. (28).

$$(\sigma_n)_I = \frac{A_C}{A_I}(\sigma_n)_H = \frac{D_{oH}^2 - (D_{oH} - 2t_H - 2t_I)^2}{(D_{oH} - 2t_H)^2 - (D_{oH} - 2t_H - 2t_I)^2} \cdot (\sigma_n)_H \tag{28}$$
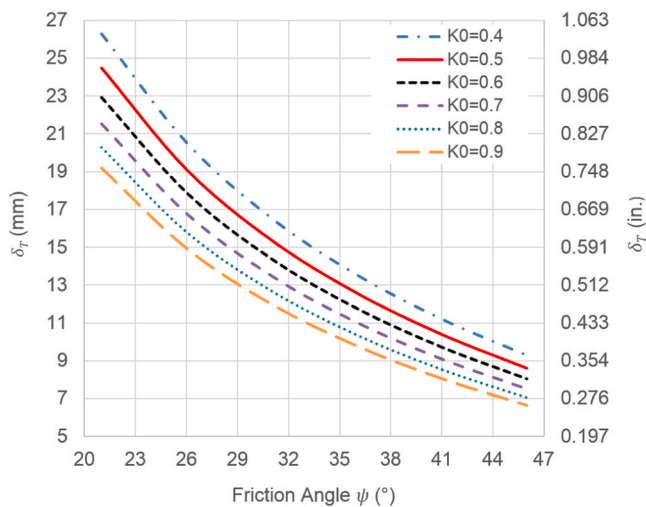
(a)

(b)

Fig. 13. Variations of the total axial deformation of the system (δ_T) with (a) coefficient of lateral earth pressure at rest and the friction angle between the soil and the host pipe, (b) pipe burial depth and the effective unit weight of the soil.
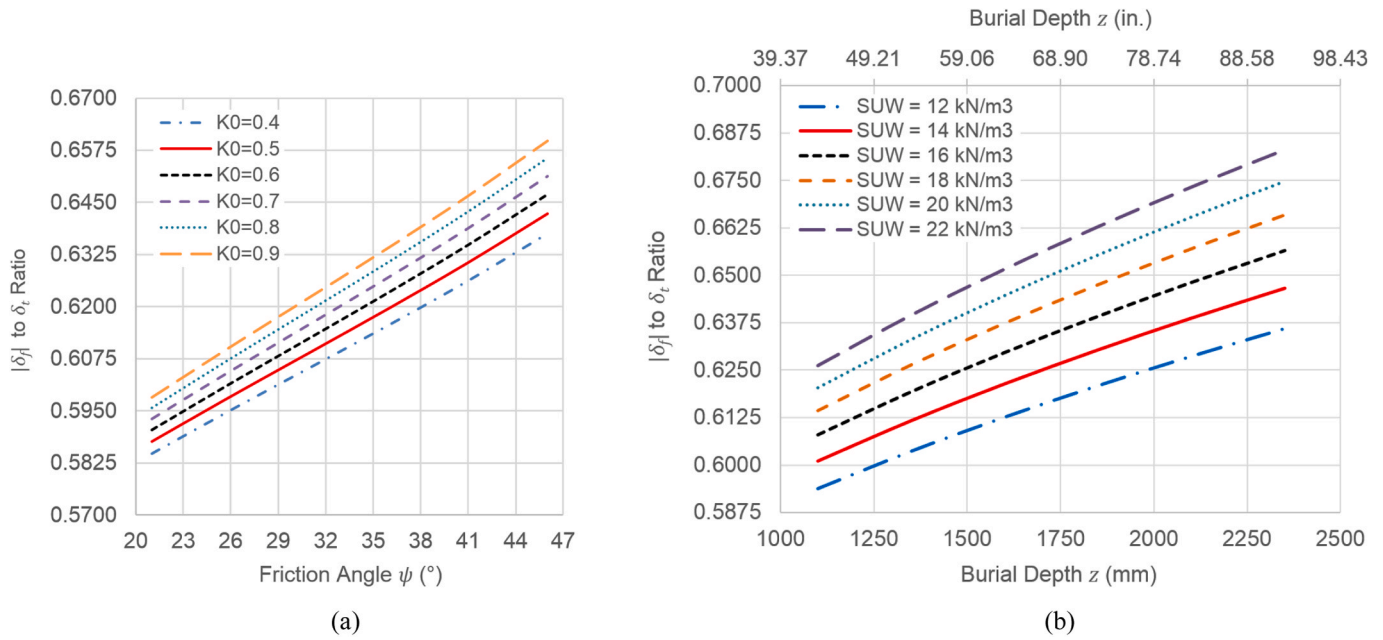
Fig. 14. Variations of the $\left|\delta_f\right|/\delta_t$ ratio with the (a) K_0 and ψ, (b) z and γ'..
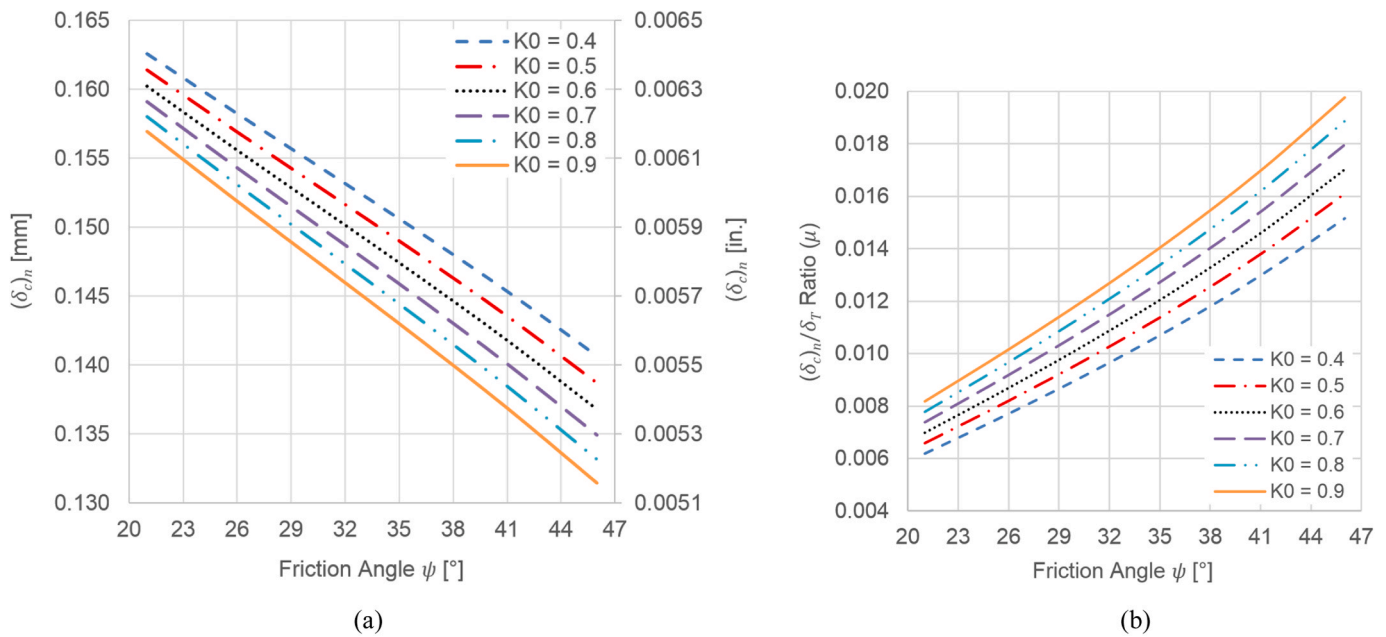

Fig. 15. Effects of K_0 and ψ on (a) nominal discontinuity opening, and (b) nominal discontinuity opening to total displacement ratio.

2.2.3. Average axial stress along the IRP thickness

Average axial stresses along the IRP thickness, $(\sigma_a)_I$, were obtained from a set of linear stress analyses conducted on 108 FE models with different geometrical and material characteristics. Axial stresses were extracted from the middle section of the discontinuity segment. An FE-driven parameter was then defined (η) to transform the values of $(\sigma_n)_I$ to the $(\sigma_a)_I$ values as follows.

$$(\sigma_a)_I = \eta(\sigma_n)_I \tag{29}$$

2.2.4. Hot-spot stress of IRP

After the extraction of average axial stress along the IRP thickness, the hot-spot stress (HSS) of IRP in the discontinuity segment can be obtained as follows.

$$(\sigma_{hs})_I = \text{SCF} \cdot (\sigma_a)_I \tag{30}$$

The SCF in Eq. (30) is the stress concentration factor that should be obtained from linear elastic FE analyses. The methodology for the extraction of SCFs from the FE models is discussed in Sect. 2.3.3.c. The HSS is considered as the representative value for the peak axial stress in the discontinuity segment which can be used for the fatigue analysis of IRP. The HSS-based approach is also implemented by API RP 2A-WSD [40] and DNV RP C203 [41], among others, in evaluating the fatigue performance of tubular joints.

2.2.5. General expression for the peak stress

The combination of Eq. (27)—(30) leads to the following expression for the hot-spot stress of IRP in the discontinuity segment.
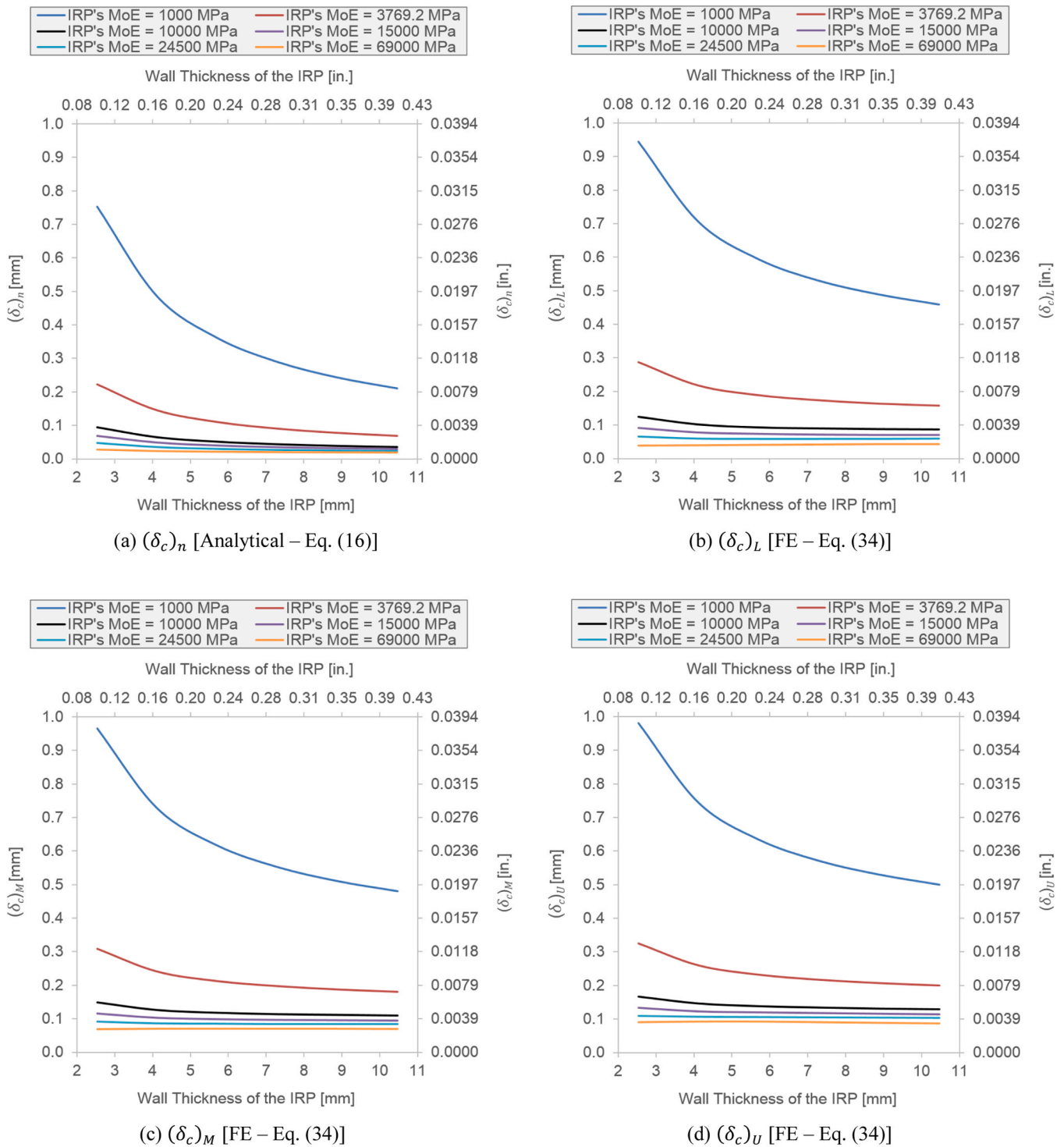
(a) $(\delta_c)_n$ [Analytical – Eq. (16)]

(b) $(\delta_c)_L$ [FE – Eq. (34)]

(c) $(\delta_c)_M$ [FE – Eq. (34)]

(d) $(\delta_c)_U$ [FE – Eq. (34)]

Fig. 16. Variations of nominal and actual discontinuity openings with IRP's wall thickness (t_I) and MoE (E_I) [$c = 12.7$ mm (0.5 in.)].

$$(\sigma_{hs})_I = \text{SCF} \cdot \eta \cdot \frac{D_{oH}^2 - (D_{oH} - 2t_H - 2t_I)^2}{(D_{oH} - 2t_H)^2 - (D_{oH} - 2t_H - 2t_I)^2}$$

$$\cdot \frac{\left[\alpha_I c + \frac{E_I A_I \alpha_I + E_H A_H \alpha_H}{E_I A_I + E_H A_H}(L - c)\right]\Delta T - \frac{(1+K_0)\gamma' z\tan\psi\pi D_{oH}}{8(E_I A_I + E_H A_H)}(L - c)^2}{\left[\frac{L - c}{E_I A_I + E_H A_H} + \frac{c}{E_I A_I}\right](A_I + A_H)} \tag{31}$$

where values of the parameters SCF and η are specified based on the results of stress analyses conducted on 108 FE models with different

geometrical and material properties.

2.3. FE modelling and analysis

2.3.1. Boundary conditions, mesh, and IRP/host pipe interface

FE-based software package ANSYS [42] was used for the numerical modelling and analysis. One end of the pipe was set as fully fixed and the other end was left free to simulate the end conditions of the analytical model described in Sect. 2.1.1 and Fig. 2a. Due to the symmetry in geometry and loading of the pipe, in order to reduce the computational
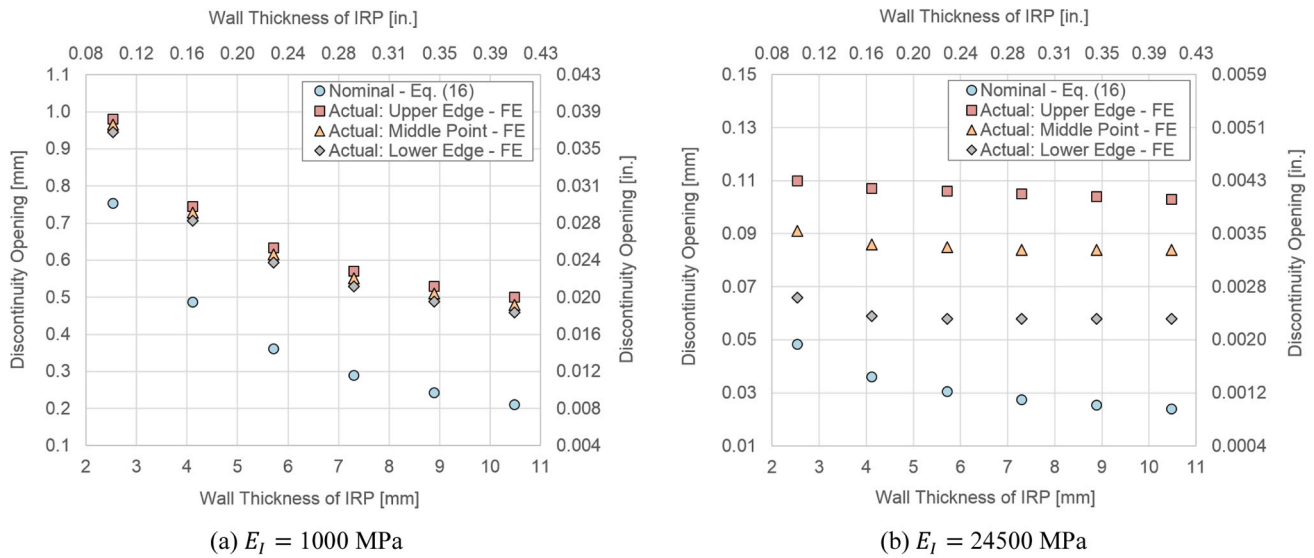
Fig. 17. Comparison of nominal and actual values of discontinuity opening for small and large values of IRP's MoE [$c = 12.7$ mm (0.5 in.)].

Table 10
The minimum and maximum values of the parameters ϕ_U, ϕ_M, and ϕ_L.

Discontinuity class	Parameter	Minimum value	Maximum value
Type I	ϕ_U	1.651	7.677
($c = 6.35$ mm)	ϕ_M	1.610	5.865
	ϕ_L	1.559	3.199
Type II	ϕ_U	1.303	4.638
($c = 12.7$ mm)	ϕ_M	1.282	3.679
	ϕ_L	1.255	2.293
Type III	ϕ_U	1.008	1.227
($c = 152.4$ mm)	ϕ_M	1.007	1.164
	ϕ_L	1.005	1.071

time, only 1/4 of the entire tubular section was modelled where appropriate symmetric boundary conditions were defined on the symmetry planes (Fig. 3a).

SOLID185 elements were used to model the host pipe and the IRP. This element type has compatible displacements and is well-suited to model curved boundaries. It is defined by eight nodes having three degrees of freedom per node and may have any spatial orientation. A sub-zone mesh generation scheme was used during the FE modelling. The entire pipe was divided to several zones according to computational requirements. The mesh of each zone was generated separately and then the mesh of the entire system was produced by merging the meshes of all the sub-zones. This scheme can feasibly control the mesh quantity and quality and avoid badly distorted elements (Fig. 3b). Before carrying out the 180 FE analyses for the parametric study, a mesh convergence check was conducted using different mesh densities in order to make sure that the results are not affected by an inadequate mesh size.

When there is no debonding at the IRP-host pipe interface, IRP and host pipe are adhered to each other along the entire interface. Hence, they cannot slide on each other, they do not separate from each other, and there is no gap between them. "Glue" condition was administered between IRP and host pipe to simulate fully bonded parts of the model.

2.3.2. Loading and analysis

According to the discussion in Sect. 2.1.5, in a mechanical FE model incorporating the soil friction, the length of the pipe cannot be specified arbitrarily. Instead, the value of f_u should be calculated first using Eq. (14), and then the obtained value must be used in Eq. (20)—(23) to calculate the required pipe length (L). Afterwards, calculated value for L, should be used in Eq. (15) to obtain the axial displacement (δ_T) that must be applied on cross sections of IRP and host pipe at free end of the pipe in

the mechanical FE model in order to simulate the axial response of the system subjected to the temperature change.

The host pipe was assumed to be API 5L X42 steel with the MoE, Poisson's ratio, and CTE of 210700 MPa (30.56 $\times 10^3$ ksi) [43], 0.3 [43], and 12×10^{-6} 1/°C (6.7 $\times 10^{-6}$ 1/°F) [44], respectively. A fixed value of 0.23 [45] was assigned to the Poisson's ratio of IRP. Different values assigned to the MoE of IRP for the linear analyses are discussed in Sect. 2.4.2. For the nonlinear analyses, ALTRA10® was selected as the IRP material; since it has been suggested as a solution for the rehabilitation of water pipelines [46] and its nonlinear stress-strain curve is available. The MoE and CTE for ALTRA10® were set to be 3769.2 MPa (546.8 ksi) [45] and 45×10^{-6} 1/°C (25 $\times 10^{-6}$ 1/°F) [47], respectively.

Axial stress-strain curves of the host pipe and IRP are shown in Fig. 4. Depicted curves are based on the true stress and true strain values. Following equations were used to transform engineering stress-strain data to the corresponding true values.

$$\sigma_{\text{true}} = \sigma_{\text{eng}}\left(1 + \varepsilon_{\text{eng}}\right) \tag{32}$$

$$\varepsilon_{\text{true}} = \ln\left(1 + \varepsilon_{\text{eng}}\right) \tag{33}$$

Engineering stress-strain curves for steel host pipes and ALTRA10® IRP were referred from Lee et al. [43] and CDCQ [45], respectively. Both small-displacement and large-displacement formulations were considered for the nonlinear analyses and the results were compared. In a large-displacement analysis, stiffness of the system is recalculated as the structure experiences the deformation. However, in a small-displacement model, no matter how much the structure deforms, the original stiffness is still used.

2.3.3. Calculation of target dimensionless parameters

2.3.3.1. Calculation of parameters ϕ_U, ϕ_M, and ϕ_L. Axial displacements at the upper, middle, and lower points of the host pipe thickness were extracted from the FE model (Fig. 5) to calculate the values of actual discontinuity opening at these positions using Eq. (34). Afterwards, calculated values were divided by the nominal discontinuity opening, given by Eq. (16), to obtain the values of ϕ_U, ϕ_M, and ϕ_L (Eq. (35)).

$$(\delta_c)_U = \delta_{1U} - \delta_{2U} \quad ; \quad (\delta_c)_M = \delta_{1M} - \delta_{2M} \quad ; \quad (\delta_c)_L = \delta_{1L} - \delta_{2L} \tag{34}$$

$$\phi_U = \frac{\delta_{1U} - \delta_{2U}}{\mu\delta_T} \quad ; \quad \phi_M = \frac{\delta_{1M} - \delta_{2M}}{\mu\delta_T} \quad ; \quad \phi_L = \frac{\delta_{1L} - \delta_{2L}}{\mu\delta_T} \tag{35}$$
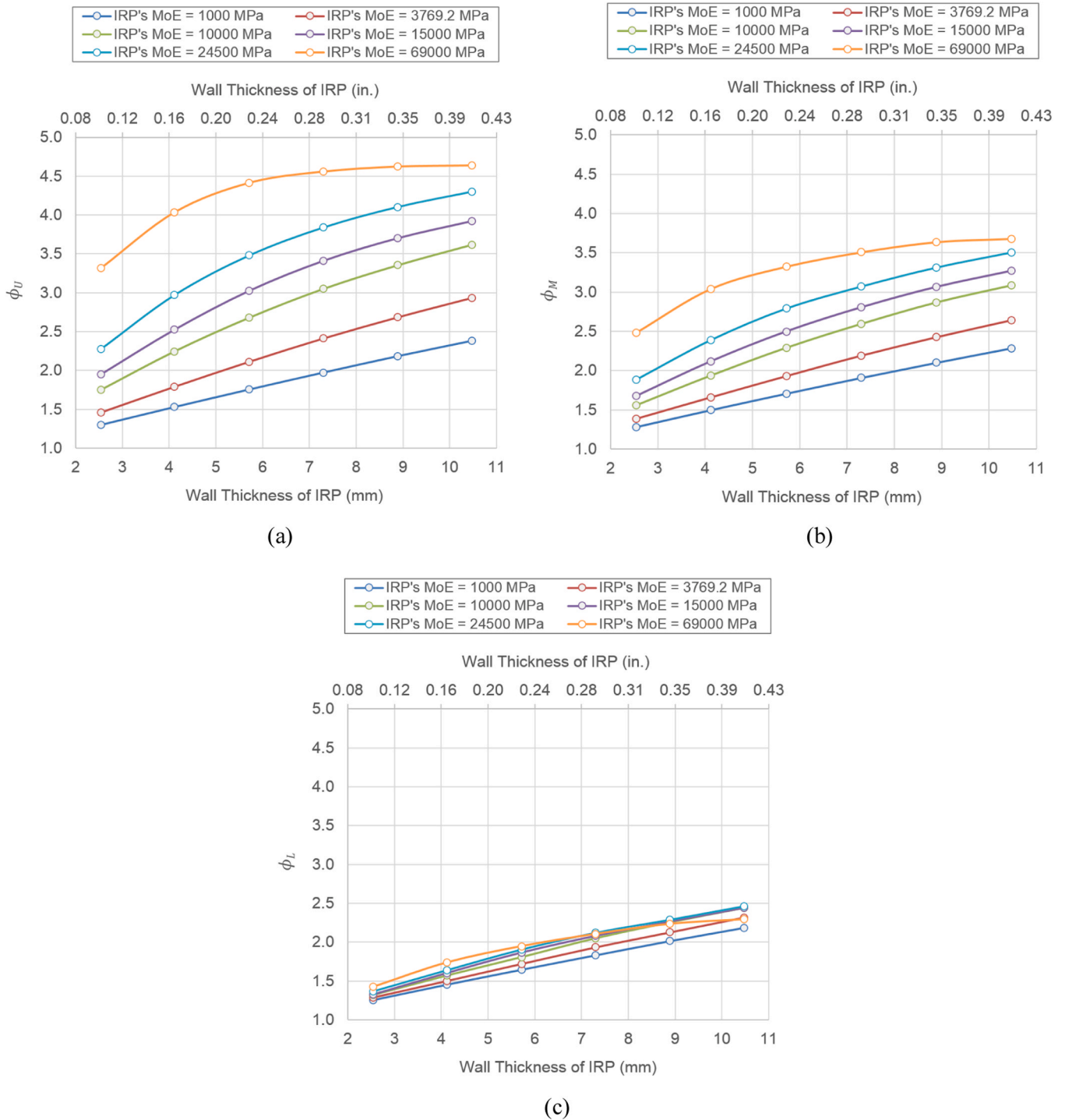
Fig. 18. Effects of the wall thickness and MoE of IRP on: (a) ϕ_U, (b) ϕ_M, (c) ϕ_L [$c = 12.7$ mm (0.5 in.)].

where δ_{1U}, δ_{2U}, δ_{1M}, δ_{2M}, δ_{1L}, and δ_{2L} are axial displacements at the two sides of the discontinuity segment, as depicted in Fig. 5.

2.3.3.2. Calculation of the parameter η. Axial stresses along the IRP thickness at the middle section of the discontinuity segment were extracted first from the FE model (Fig. 5) to calculate the average axial stress along the IRP thickness using Eq. (36a). Afterwards, calculated value was divided by the nominal axial stress of IRP, given by Eq. (28), to obtain the value of the parameter η (Eq. (36b)).

$$(\sigma_a)_I = \frac{1}{k} \sum_{i=1}^{k} \sigma_{mi} \quad \text{(a)} \quad \rightarrow \quad \eta = \frac{A_I}{kA_C(\sigma_n)_H} \sum_{i=1}^{k} \sigma_{mi} \quad \text{(b)} \tag{36}$$

where k is the number of nodes along the IRP thickness, and σ_{mi} is the axial stress in the ith node along the IRP thickness at the middle section of the discontinuity segment as depicted in Fig. 5.

2.3.3.3. Calculation of the stress concentration factor (SCF). According to Eq. (30), the SCF is defined as:
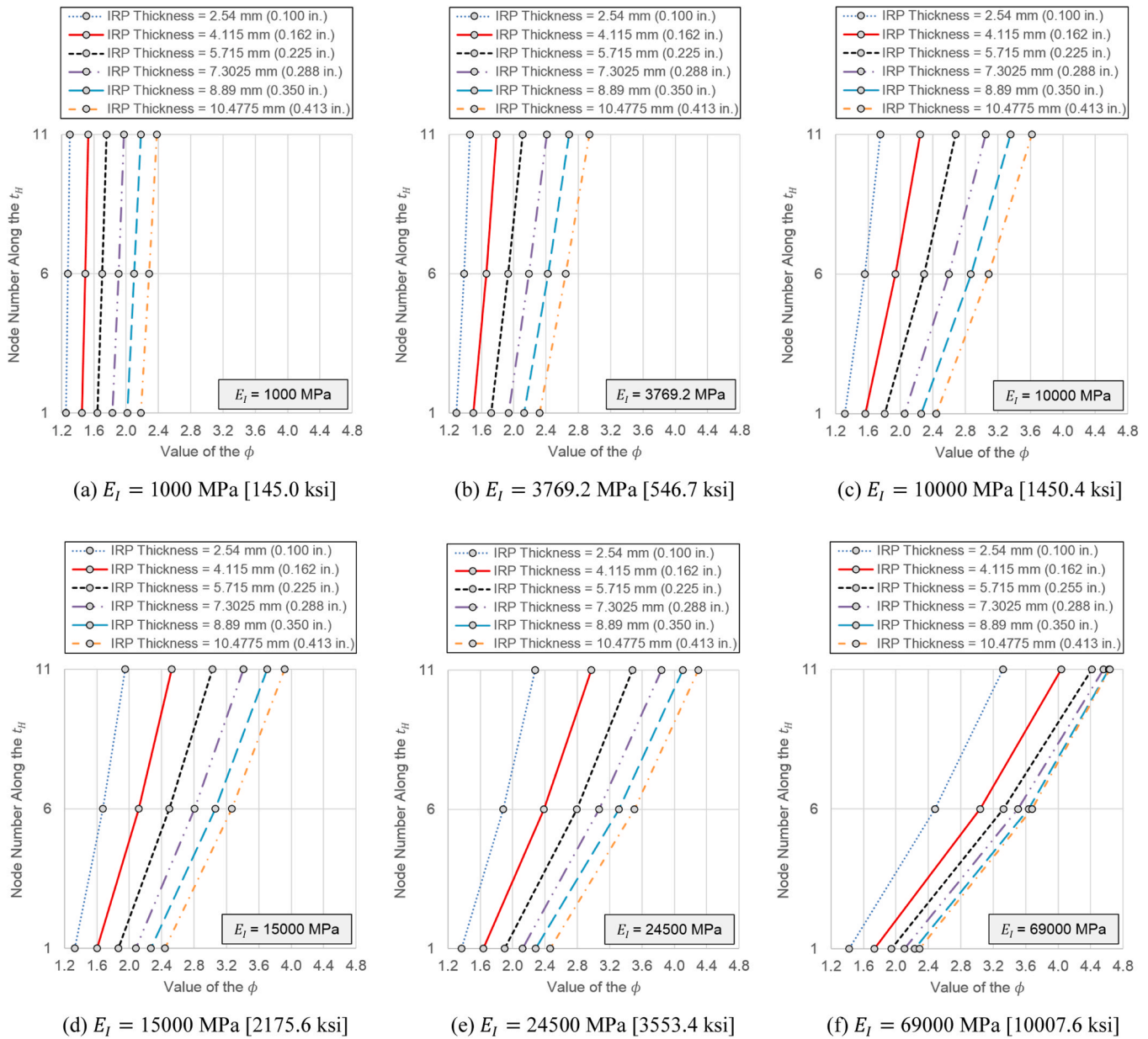
Fig. 19. Effects of the wall thickness and MoE of IRP on variations of the actual to nominal discontinuity opening ratio (ϕ) along the thickness of the host pipe [$c = 12.7$ mm (0.5 in.)].

$$\text{SCF} = \frac{(\sigma_{hs})_I}{(\sigma_a)_I} \tag{37}$$

where $(\sigma_{hs})_I$ and $(\sigma_a)_I$ are the hot-spot stress (HSS) and average axial stress of IRP along the thickness, respectively.

The HSS at discontinuity's lower edge was of interest. The reason is that, as shown in Fig. 6, peak axial stress in IRP system always occurs at this position. To determine the HSS, the stress at the discontinuity edge should be extracted from the stress field outside the region influenced by the local edge geometry [48,49]. The HSS obtained in this way is a function of the global geometry of the system rather than the very local geometry of the notch. The location from which the stresses must be extrapolated, called the extrapolation region, depends on the dimensions of the system [50]. According to the recommendations of HSE OTH 354 [51] for acrylic tubular joints without the weld and proposed extrapolation method by the IIW-2259–15 [52], the first extrapolation point was selected to be at a distance of $0.4t_I$ from the edge, and the second point was selected to be $0.6t_I$ further from the first point, where t_I

is the thickness of IRP. The HSS was obtained by the linear extrapolation of the geometric stresses at these two points to the edge position; as follows (Fig. 5).

$$\sigma_{hs} = \frac{1}{0.6}\sigma_{a1} - \frac{0.4}{0.6}\sigma_{a2} \tag{38}$$

where σ_{a1} and σ_{a2} are axial stresses at the first and second extrapolation points, respectively.

Substitution of $(\sigma_a)_I$ from Eq. (36a) and σ_{hs} from Eq. (38) into Eq. (37) results in the following expression for the calculation of SCF in IRP systems.

$$\text{SCF} = \frac{k(\sigma_{a1} - 0.4\sigma_{a2})}{0.6\sum\limits_{i=1}^{k}\sigma_{mi}} \tag{39}$$

In order to retain the consistency of the mesh densities in models with different geometrical properties, the value of the k in Eq. (39)
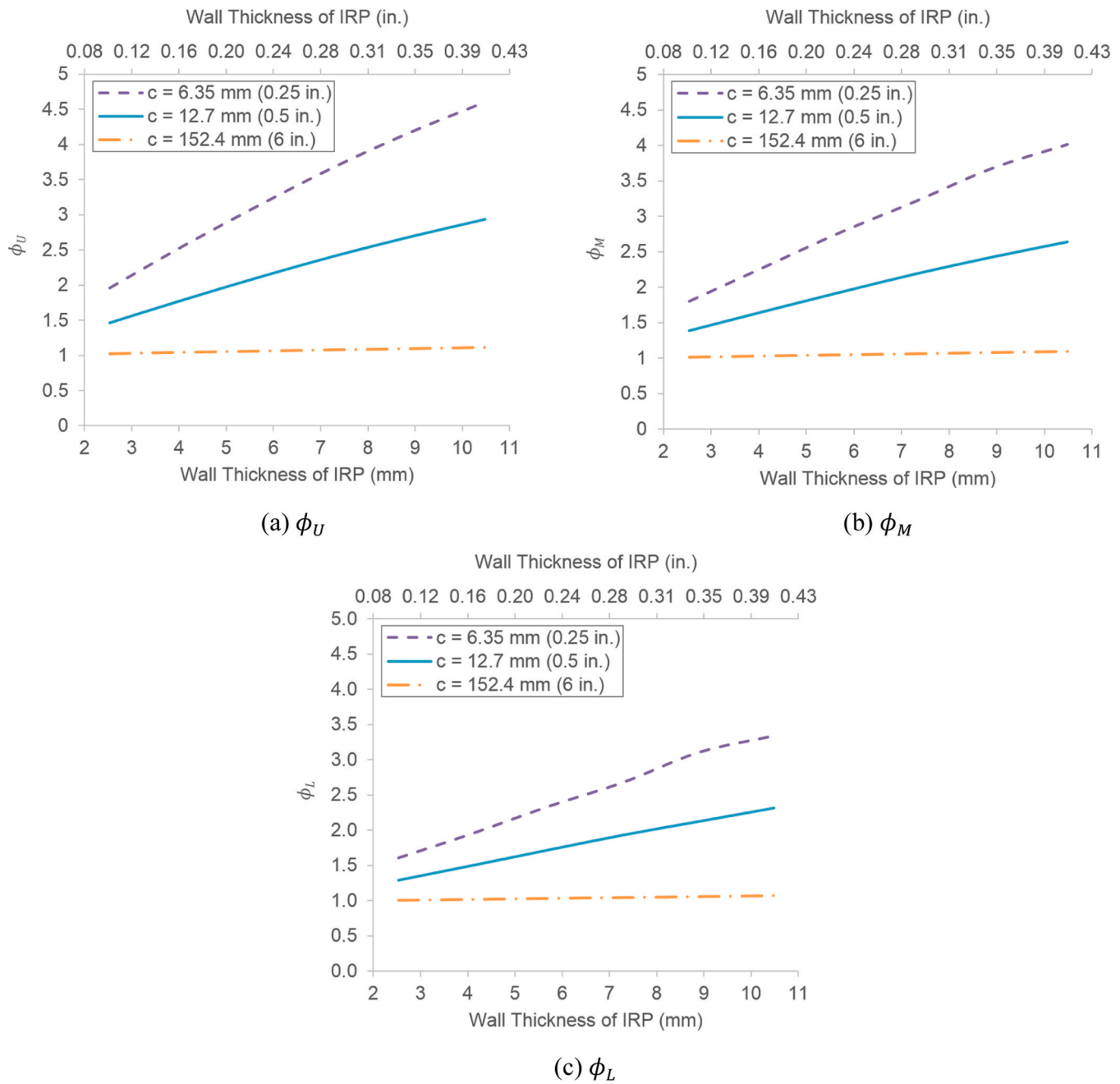
(a) ϕ_U

(b) ϕ_M

(c) ϕ_L

Fig. 20. Variations of ϕ_U, ϕ_M, and ϕ_L with the IRP thickness for different values of the discontinuity width [$E_I = 3769.2$ MPa (546.7 ksi)].

should be a function of IRP thickness and was equal to 4, 7, 10, 13, 16, and 21 for τ values of 0.4, 0.65, 0.9, 1.15, 1.4, and 1.65, respectively. The parameter τ is defined as the IRP to host pipe thickness ratio (t_I/t_H).

2.3.4. Verification of the developed FE model

2.3.4.1. Examination of nominal axial stress and discontinuity opening due to the temperature change. Nominal axial stress of IRP and nominal value of the discontinuity opening were extracted from a sample FE model, called LS03, subjected to the axial displacement (Eq. (15)) equivalent of a $\Delta T = 27.8$ °C (50 °F) temperature change. Geometrical and material properties of the LS03 model are listed in Table 1. Axial stress at the central node along the IRP thickness at the middle section of the discontinuity segment was extracted from the FE model as the representative nominal value for the axial stress of IRP. Nominal discontinuity opening was extracted from the FE model by calculating the differences

between the nodal displacements of IRP at the two ends of the discontinuity segment and then averaging them along the IRP thickness. Analytical solutions for nominal discontinuity opening and nominal axial stress of IRP were obtained from Eqs. (16) and (28), respectively. Verification results summarized in Table 2 indicate that there is a very good agreement between the FE results and analytically predicted values for both axial stress and discontinuity opening.

2.3.4.2. Examination of stresses and deformations due to the internal pressure. The validity of FE model developed to study the effect of internal pressure on the axial response of the system was verified by comparing the analytical results obtained from closed-form solutions and the FE results extracted from a host-pipe-only case with $\Delta T = 0$ °C and an internal pressure of 1 MPa (0.145 ksi). Geometrical and material properties of the host pipe are as listed in Table 1. Circumferential/hoop stress (σ_θ), axial/longitudinal stress (σ_l), and radial stress (σ_r) in the host
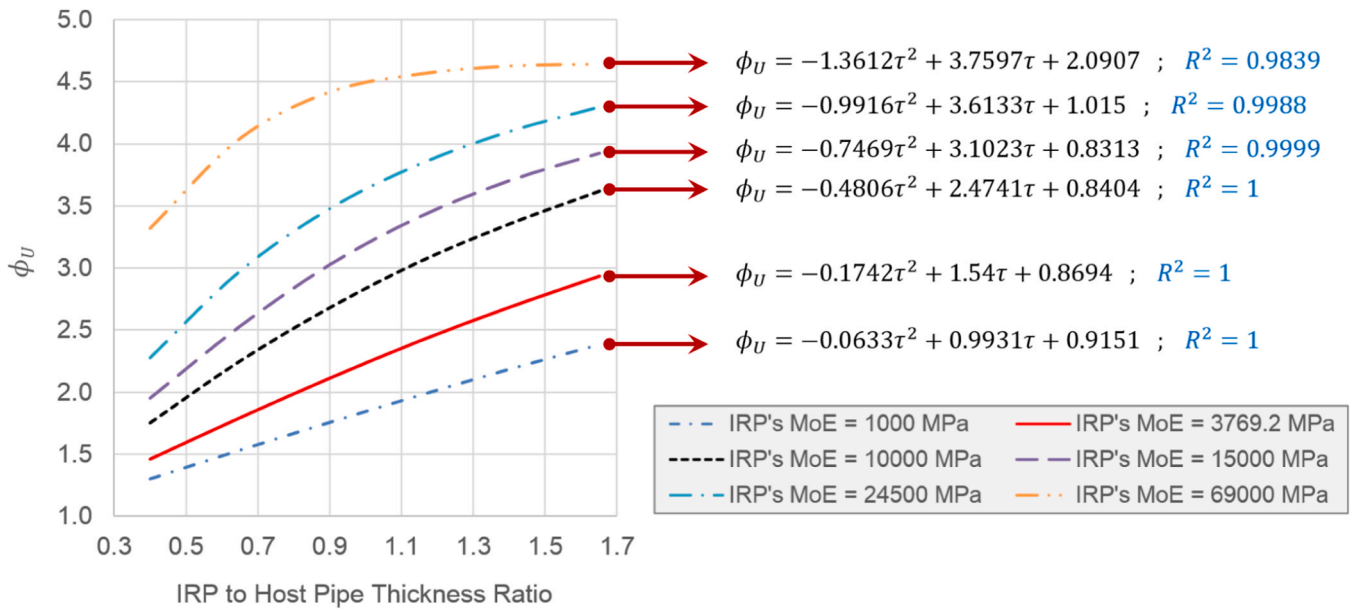
Fig. 21. An example of the conducted regression analyses: Formulation of ϕ_U as a function of τ (Eq. (49)) for different values of IRP's MoE — Type II discontinuity (c = 12.7 mm [0.5 in.]).
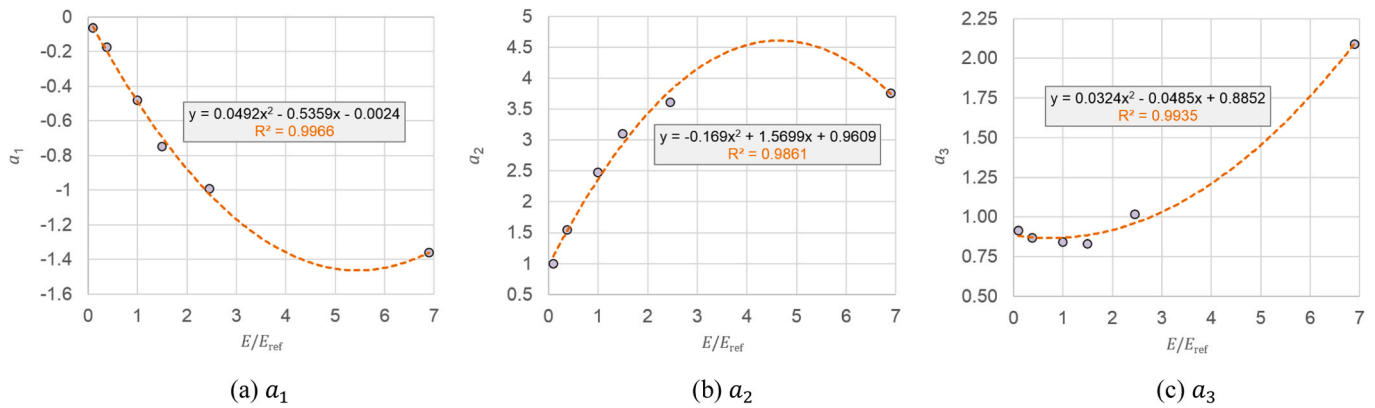

(a) a_1 (b) a_2 (c) a_3

Fig. 22. An example of the conducted regression analyses: Formulation of a_1, a_2, and a_3 as a function of e (Eq. (52)) — Type II discontinuity (c = 12.7 mm [0.5 in.]).

pipe due to the internal pressure of the pipeline are calculated by Eq. (40)—(42), respectively.

$$\sigma_\theta = \frac{p_i D_{iH}}{2t_H} \tag{40}$$

$$\sigma_l = \nu\sigma_\theta \tag{41}$$

$$\sigma_r = -p_i \tag{42}$$

where p_i is the internal pressure of the pipeline; D_{iH} is the inner diameter of the host pipe; t_H is the wall thickness of the host pipe; and ν is the Poisson's ratio of the host pipe's material which was assumed to be API 5L X42 steel.

Assuming a linear material behaviour, total axial deformation of the system can be calculated as follows.

$$\delta_T = \delta(x)\big|_{x=L} = \int_0^L \varepsilon_l(x)dx = \int_0^L \frac{\sigma_l}{E_H}dx = \int_0^L \frac{\nu\sigma_\theta}{E_H}dx = \frac{\nu p_i D_{iH}x}{2E_H t_H}\bigg|_{x=0}^{x=L}$$

$$= \frac{\nu p_i D_{iH}L}{2E_H t_H} \tag{43}$$

Verification results presented in Table 3 show that the developed FE model is accurate enough to provide valid results.

2.3.4.3. Comparison of discontinuity opening obtained from the FE analysis with the experimental data. An experimental study was conducted at the University of Colorado Boulder. Two specimens consisting of steel host pipe and ALTRA10® IRP were tested (S01 and S02). Geometrical and material properties of the specimens are listed in Table 4. Specimens were axially tested in a horizontal position (Fig. 7). Actuators with the capacity of 500 kN (112.4 kips) and 1000 kN (224.8 kips) were used to test S01 and S02 specimens, respectively. In loading, specimens were supported by one or two supports with low friction pads to avoid potential side-loading because of the specimen weight. Tensile loading was performed wherein the load was transferred to the specimens through the flanges with rods. Traffic and parallel excavation loadings were also simulated in the lab and specimens were subjected to 600,000 fatigue cycles before conducting the pull-push tests. The prior bending tests might have led to some degree of debonding. Compared to the FE model of the S01 specimen, a larger unbonded length was required for the FE model of the S02 specimen to simulate the experimental tests. This finding is in agreement with the condition of the specimens used for the tests. The reason is that the parallel excavation was reflective of a considerably larger soil displacement for the S02 specimen compared to the S01. Hence, despite smoother geometry of the specimen with the wider discontinuity, larger debonding before the first axial test was

Table 11
Values of coefficients ϑ_i, ξ_i, and ω_i to be used in Eq. (52)—(54).

Coefficient	Discontinuity class		
	Type I: Fracture ($c = 6.35$ mm)	Type II: Joint ($c = 12.7$ mm)	Type III: Aging ($c = 152.4$ mm)
ϑ_{U1}	0.1009	0.0492	0
ϑ_{U2}	-0.3219	-0.169	-0.0041
ϑ_{U3}	0.059	0.0324	-0.0005
ξ_{U1}	-1.0154	-0.5359	0
ξ_{U2}	2.8245	1.5699	0.0288
ξ_{U3}	0.0175	-0.0485	0.0245
ω_{U1}	-0.0413	-0.0024	0
ω_{U2}	1.8329	0.9609	0.0572
ω_{U3}	0.8507	0.8852	0.9845
ϑ_{M1}	0.0567	0.0282	0
ϑ_{M2}	-0.1931	-0.1018	-0.0027
ϑ_{M3}	0.0376	0.0183	-0.0002
ξ_{M1}	-0.6074	-0.3234	0
ξ_{M2}	1.7545	0.9716	0.0198
ξ_{M3}	-0.0329	-0.0314	0.0132
ω_{M1}	-0.0465	-0.025	0
ω_{M2}	1.6363	0.9158	0.0506
ω_{M3}	0.9272	0.9002	0.9857
ϑ_{L1}	0.0164	0.0176	0
ϑ_{L2}	-0.0582	-0.0448	-0.0002
ϑ_{L3}	0.017	0.0111	0.0004
ξ_{L1}	-0.2084	-0.1409	0
ξ_{L2}	0.5436	0.3628	0.0013
ξ_{L3}	-0.1071	-0.0682	-0.0015
ω_{L1}	-0.0624	-0.026	0
ω_{L2}	1.4825	0.8375	0.0069
ω_{L3}	0.9758	0.9274	0.9876

possible or even likely in S02 specimen. Comparing the values of the discontinuity opening obtained from the FE analysis with the experimental data (Table 5) lends some support to the validity of the developed FE model.

2.4. Details of parametric study

2.4.1. Parametric study on effects of internal pressure, burial depth, soil properties, and material/geometric nonlinearities

Two levels of seasonal temperature changes were considered in the present research. The first value was $\Delta T = 27.8\,°C$ (50 °F) as the representative of the maximum seasonal temperature changes of the pipelines in New York State and other parts of the Northeast US which is in the range of $\Delta T = 22—27.8\,°C$ (40—50 °F) [35,53]. The second value was $\Delta T = 55.0\,°C$ (99 °F) which is the representative of the maximum temperature changes of the pipelines in the entire United States. This amount of temperature variation can occur, for example, in Arizona desert [55].

Collectively, 132 sets of analytical calculations plus 72 linear and nonlinear FE analyses were carried out to investigate the effects of the pipeline's internal pressure/burial depth, soil properties, and material/geometric nonlinearities on the axial stresses and displacements of the IRP system with a host-pipe circumferential discontinuity due to seasonal temperature variations. Different values assigned to various characteristics of the model are listed in Table 6. These values cover the practical ranges expected to be typically found in IRP systems used for the rehabilitation of buried pipelines.

2.4.2. Parametric study to characterize the dimensionless modification factors

A total of 108 FE models were generated and analysed to investigate the effects of geometrical and material characteristics on the values of parameters ϕ_U, ϕ_M, ϕ_L, η, and SCF in order to formulate the axial stresses and deformations of IRP due to seasonal temperature changes. Three variables were considered: wall thickness of IRP, MoE of IRP, and discontinuity width. Different values assigned to geometrical and ma-

terial characteristics of the system are listed in Table 7 covering the practical ranges expected for IRP systems.

To represent a circumferential fracture due to the buckling, impact or fatigue-induced progressive crack propagation, a discontinuity width equal to 6.35 mm (1/4 in.) was selected (Type I). To represent a circumferential discontinuity at bell and spigot joints, the discontinuity width was selected to be equal to 12.7 mm (1/2 in.) (Type II); and in order to represent a circumferential discontinuity due to the elimination of a major part of host pipe as a result of aging, the discontinuity width was selected to be equal to 152.4 mm (6 in.) (Type III).

A set of dimensionless geometrical parameters was also defined, as follows, to easily relate the behaviour of the system to its geometrical characteristics.

$$\tau = \frac{t_I}{t_H} \quad ; \quad \zeta = \frac{c}{t_H} \tag{44}$$

Selected wall thicknesses are corresponding to the τ ratios of 0.4, 0.65, 0.9, 1.15, 1.4, and 1.65; and values assigned to the discontinuity width lead to the ζ ratios of 1, 2, and 24.

3. Results and discussion

3.1. Adequate pipe length (L) for mechanical model

As discussed in Sect. 2.1.5, pipe length for mechanical model of Fig. 2a to simulate the thermal effects cannot be assigned arbitrarily. Instead, the pipe should be long enough to generate adequate soil friction to neutralize the force induced by the temperature change, so the displacement at the pipe end can reliably be assumed to be zero. Such pipe length (L) can be calculated using Eq. (20)—(23). Fig. 8 shows that the increases of the coefficient of lateral earth pressure at rest (K_0), friction angle between the soil and host pipe (ψ), effective unit weight of the soil (γ'), and burial depth of the pipe (z) all result in the decrease of the L. The reason is that according to Eq. (14), the increase of these parameters leads to the increase of mobilized soil friction per unit length of the pipe which consequently results in the decrease of the pipe length required to neutralize the force induced by the temperature change.

Fig. 9 depicts the effects of the pipeline's internal pressure and the maximum mobilized soil friction force per unit length on the pipe length in an equivalent mechanical model. Fig. 9a indicates that as the amount of the internal pressure increases, a longer pipe should be considered in the mechanical model. Fig. 9b shows that with the increase of the f_u, the internal pressure becomes less effective on the value of L. According to Fig. 9b, the maximum difference between the pipe length values with and without the consideration of internal pressure is less than 10%. For $p_i = 0$, Eq. (20)—(23) proposed in the present research for the calculation of pipe length (L) reduce to the equations previously developed by Stewart et al. [35]. Fig. 9b indicates that if the pipeline's internal pressure is between 0.25 MPa (36.3 psi) and 1 MPa (145 psi) which covers a wide range of practical applications, the average and maximum differences between the outcomes of the present formulation (Eq. (20)—(23)) and equations proposed by Stewart et al. [35] are 4% and 9%, respectively.

Fig. 10 demonstrates the effects of the pipe displacement required to mobilize the full soil resistance (δ_u) and the maximum mobilized soil friction force per unit length (f_u) on the value of the pipe length in an equivalent mechanical model. According to Fig. 10a, the increase of δ_u leads to the increase of the pipe length in an equivalent mechanical model. Fig. 10b shows that with the increase of f_u, the amount of δ_u becomes more effective on the value of L. According to Fig. 10b, if δ_u ranges between 0.25 and 4 mm, the maximum difference between the pipe lengths in mechanical models is around 25%.

A tornado diagram is provided in Fig. 11 comparing the effects of parameters p_i, δ_u, and f_u on the required pipe length for a mechanical FE model. The range of parameters p_i, δ_u, and f_u used for the generation of the tornado diagram shown in Fig. 11 are as follows.
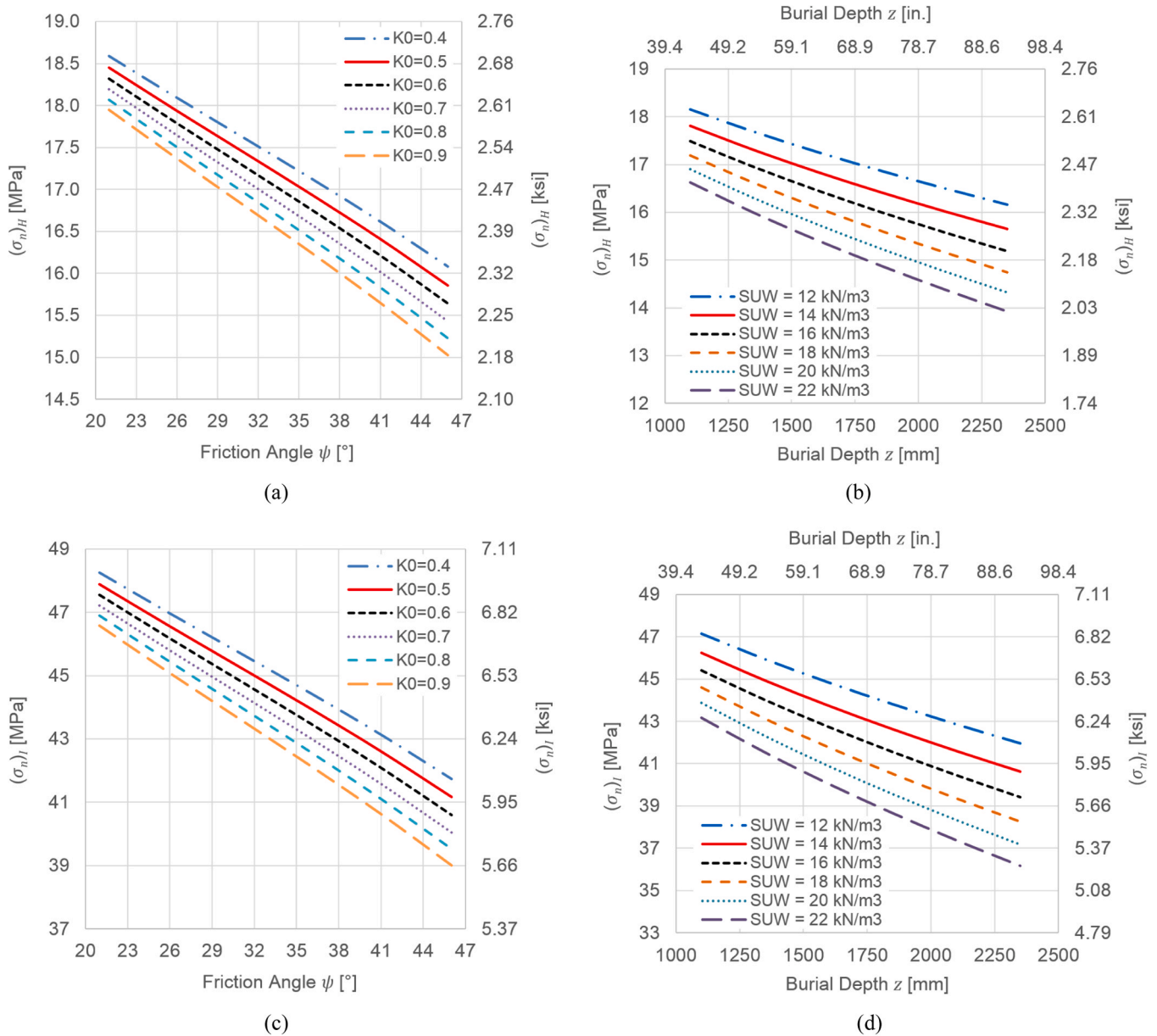
Fig. 23. Effects of K_0, ψ, z, and γ' on axial stress of the compound section ((a) and (b)) and nominal axial stress of IRP in the discontinuity segment ((c) and (d)).

$0 \leq p_i \leq 1$ MPa (145 psi)

0.25 mm (0.0098 in.) $\leq \delta_u \leq 4$ mm (0.1575 in.)

8.24 N/mm (47.05 lb/in.) $\leq f_u \leq 29.29$ N/mm (167.25 lb/in.)   (45)

Base values for the above parameters as well as the fixed values for all the other parameters required for the calculation of L using Eq. (20)—(23) are listed in Table 8. Base value of the pipe length calculated using the parameter values listed in Table 8 is 86,469 mm. Fig. 11 clearly indicates that among parameters p_i, δ_u, and f_u, the most influential parameter on the length of the pipe in a mechanical FE model is f_u, and the least effective parameter is p_i. Practical range for the parameter p_i was selected based on the recommendations of CIEST [54] and Dixon et al. [22].

In order to directly compare the effects of parameters K_0, γ', z, and ψ on the required pipe length for a mechanical FE model, f_u can be rewritten in terms of these four parameters using Eq. (14) and then substituted in Eq. (20)—(23) for the calculation of L. A tornado diagram is provided in Fig. 12 comparing the effects of parameters K_0, γ', z, ψ, p_i, and δ_u on the value of the required pipe length (L). The range of

parameters K_0, γ', z, ψ, p_i, and δ_u used for the generation of the tornado diagram shown in Fig. 12 are as defined in Eqs. (45) and (46). Base values for variable parameters as well as the fixed values for all the other parameters required for the calculation of L using Eq. (20)—(23) are listed in Tables 8 and 9. Base value of the pipe length calculated using the parameter values listed in Tables 8 and 9 is 86,469 mm (3404.29 in.).

$0.4 \leq K_0 \leq 1$

12×10^{-6} N/mm³ (0.0442 lb/in³) $\leq \gamma' \leq 22 \times 10^{-6}$ N/mm³ (0.081 1 lb/in³)

1080 mm (42.52 in.) $\leq z \leq 2350$ mm (92.52 in.)

$21° \leq \psi \leq 46°$ (46)

According to Fig. 12, the most and the least effective parameters on the required pipe length for a mechanical FE model are the friction angle at the interface between the soil and the host pipe (ψ) and the internal pressure of the pipeline (p_i), respectively. Practical range for the parameter ψ was selected based on the recommendations of Meidani et al. [56]. Effectiveness (*Eff*) of the six considered parameters on the
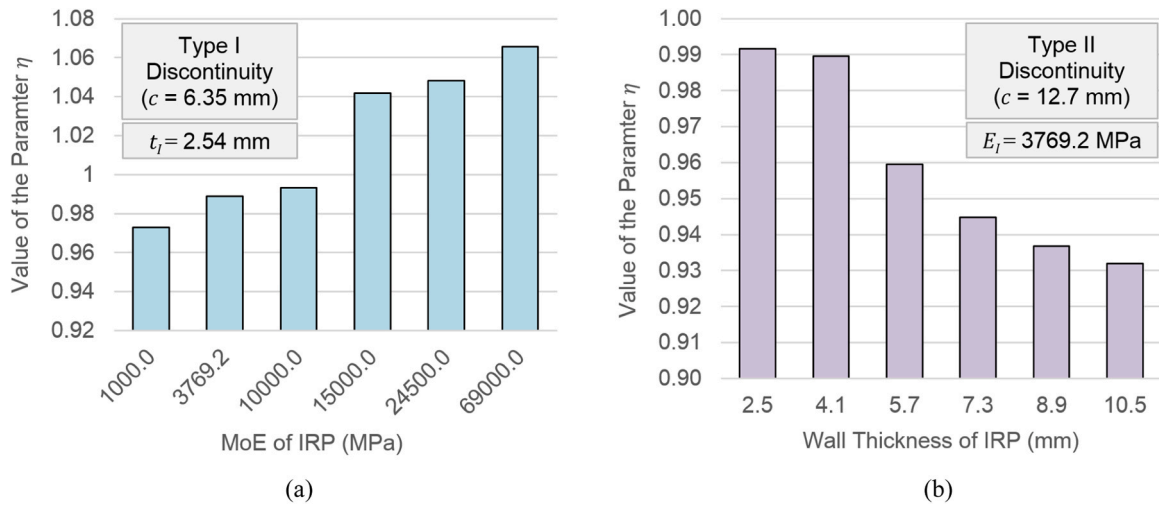
Fig. 24. Variations of the parameter η with (a) IRP's MoE (E_I), (b) IRP's wall thickness (t_I).
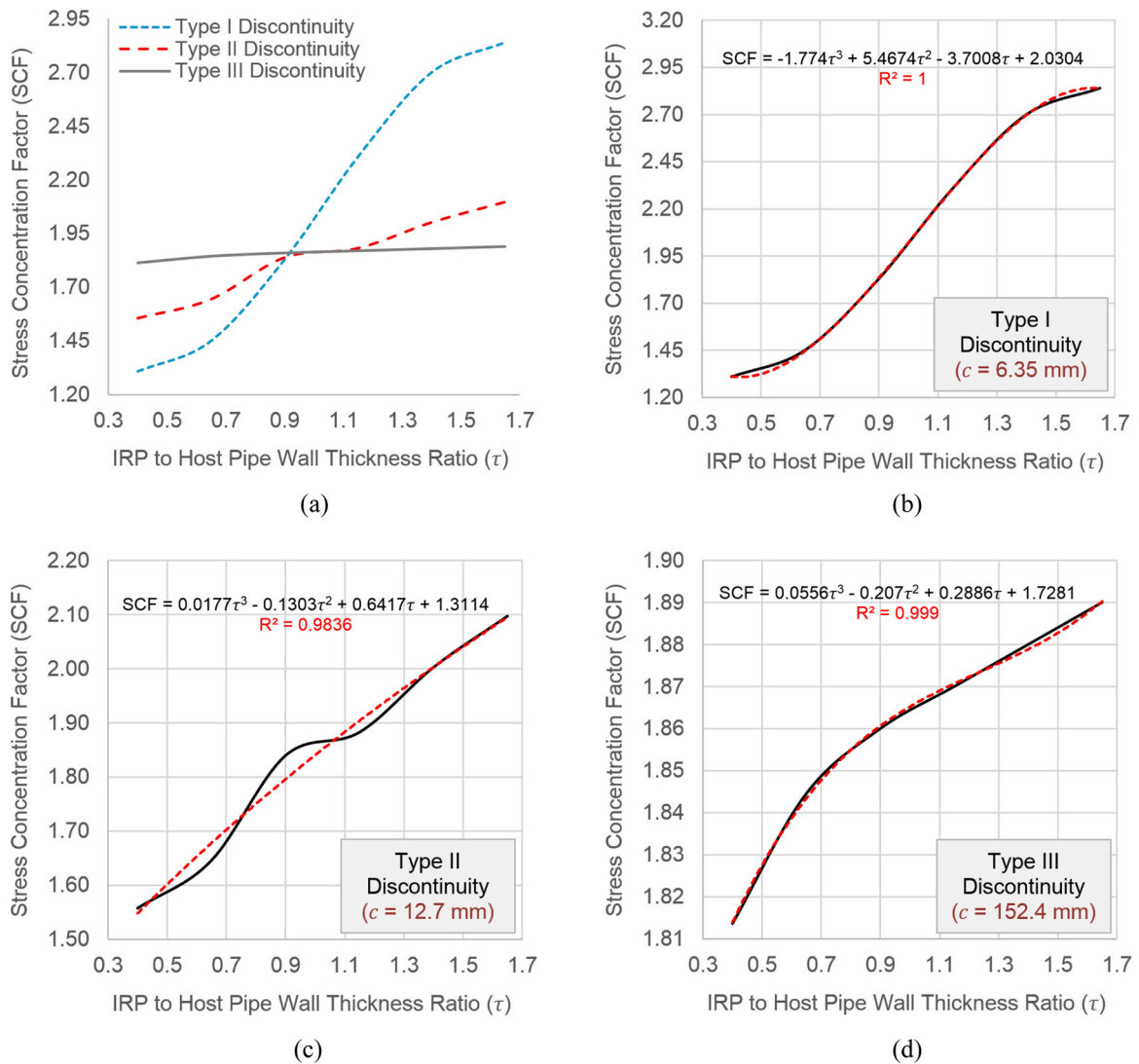

Fig. 25. (a) Variations of SCFs due to the change of τ and its interaction with ζ, (b)—(d) Curves fitted to the SCF data of Types I, II, and III discontinuity.

Table 12

Values of input parameters for studying the effects of material and geometric nonlinearities.

Parameter	Symbol	Unit	Value (s)
Friction angle at the soil/host pipe interface	ψ	°	21, 26, 31, 36, 41, 46
Temperature change [35,53,55]	ΔT	°C	27.8, 55.0
MoE of IRP [45]	E_I	MPa	3769.2
Poisson's ratio of IRP [45]	ν_I	-	0.23
CTE of IRP [47]	α_I	1/°C	45×10^{-6}
MoE of the host pipe [43]	E_H	MPa	210700
Poisson's ratio of the host pipe [43]	ν_H	-	0.3
CTE of the host pipe [44]	α_H	1/°C	12×10^{-6}
Discontinuity width	c	mm	12.7
Wall thickness of IRP [54]	t_I	mm	4.115
Cross sectional area of IRP	A_I	mm²	3969.24
Outer diameter of the host pipe [54]	D_{oH}	mm	323.85
Wall thickness of the host pipe [54]	t_H	mm	6.35
Cross sectional area of the host pipe	A_H	mm²	6330.4
Inner diameter of the host pipe	D_{iH}	mm	311.15
Coefficient of lateral earth pressure at rest [35]	K_0	-	1
Effective unit weight of the soil [35]	γ'	N/mm³	19.6×10^{-6}
Burial depth to the pipe's centreline	z	mm	1100
Pipe displacement required to mobilize full soil resistance [35]	δ_u	mm	1
Internal pressure of the pipeline [54]	p_i	MPa	0.45

length of the pipe in a mechanical FE model is ranked as follows.

$$\{Eff\}_\psi > \{Eff\}_{\gamma'} > \{Eff\}_z > \{Eff\}_{K_0} > \{Eff\}_{\delta_u} > \{Eff\}_{p_i} \tag{47}$$

3.2. Discontinuity opening

3.2.1. Variations of axial deformations, the μ ratio, and nominal discontinuity opening with soil-related parameters

Fig. 13 indicates that the increases of the coefficient of lateral earth pressure at rest, friction angle between the soil and host pipe, effective unit weight of the soil, and burial depth of the pipe all result in the decrease of the total axial deformation of the system (δ_T) subjected to simultaneous effects of temperature change and soil friction. It can been

seen that among parameters K_0, γ', z, and ψ, the most effective term in reducing the total axial deformation is ψ implying that the most influential soil-related parameter on the axial response of the pipe subjected to the temperature change is the friction angle between the soil and host pipe. This result is in agreement with the findings of Sect. 3.1.

Fig. 14 shows the change of the $|\delta_f|/\delta_t$ ratio, calculated based on Eq. (1)—(6), with parameters K_0, ψ, z, and γ'. It can be seen that this ratio increases with the increase of all the considered parameters. The reason is that the increase of these parameters leads to the increase of mobilized soil friction which consequently increases the amount of displacement reduction due to the presence of soil ($|\delta_f|$). It can also be seen that depending on soil properties, the approximate range for the $|\delta_f|/\delta_t$ ratio is 0.58—0.68 implying that the soil friction can play a major role in reducing the axial deformation due to the temperature change and thus cannot be omitted from the analysis for the sake of simplification.

Fig. 15a clearly shows that the increase of the K_0 and/or ψ leads to the decrease of the nominal discontinuity opening, and the difference between the minimum and maximum values of the discontinuity opening is around 19%. According to Fig. 15b, with the increase of the K_0 and/or ψ, nominal discontinuity opening to total displacement ratio increases.

3.2.2. Effects of geometrical and material properties on actual discontinuity opening

Fig. 16 shows that, as expected, the increase of the thickness and/or MoE of IRP results in the decrease of both nominal and actual values of the discontinuity opening. Fig. 16 also indicates that the nominal (Eq. (16)) and actual (Eq. (34)) values of the discontinuity opening along the thickness of host pipe can be ranked as follows.

$$(\delta_c)_n < (\delta_c)_L < (\delta_c)_M < (\delta_c)_U \tag{48}$$

According to Fig. 17, for high values of the IRP's MoE, the change of IRP thickness does not have a significant effect on the values of actual discontinuity opening obtained from the FE analysis. Such behaviour is not reflected in the nominal discontinuity opening values, predicted by Eqs. (16) and (17), which consequently results in the increase of ϕ_U, ϕ_M, and ϕ_L values as the IRP thickness increases. On the contrary, for low values of the IRP's MoE, as shown in Fig. 17a, the decreases in nominal and actual discontinuity values due to the increase of IRP thickness
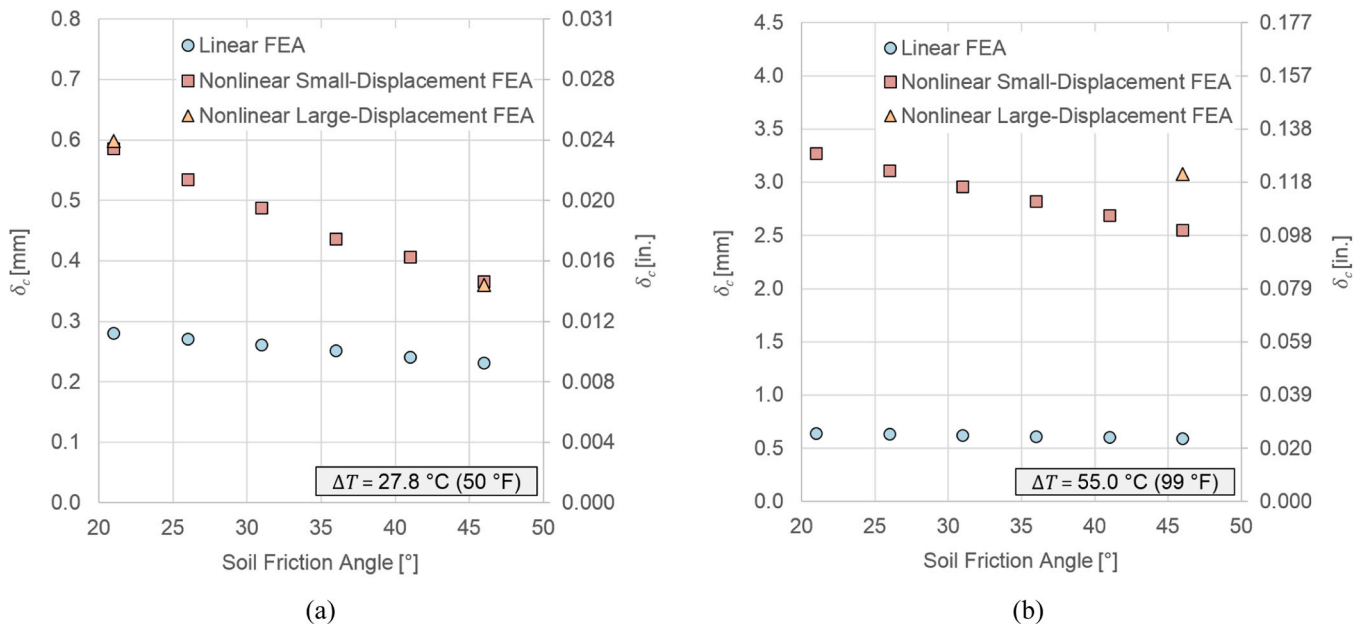

(a)

(b)

Fig. 26. Variations of actual discontinuity opening with the soil friction angle obtained from linear and nonlinear analyses for (a) $\Delta T = 27.8$ °C (50 °F), (b) $\Delta T = 55.0$ °C (99 °F).
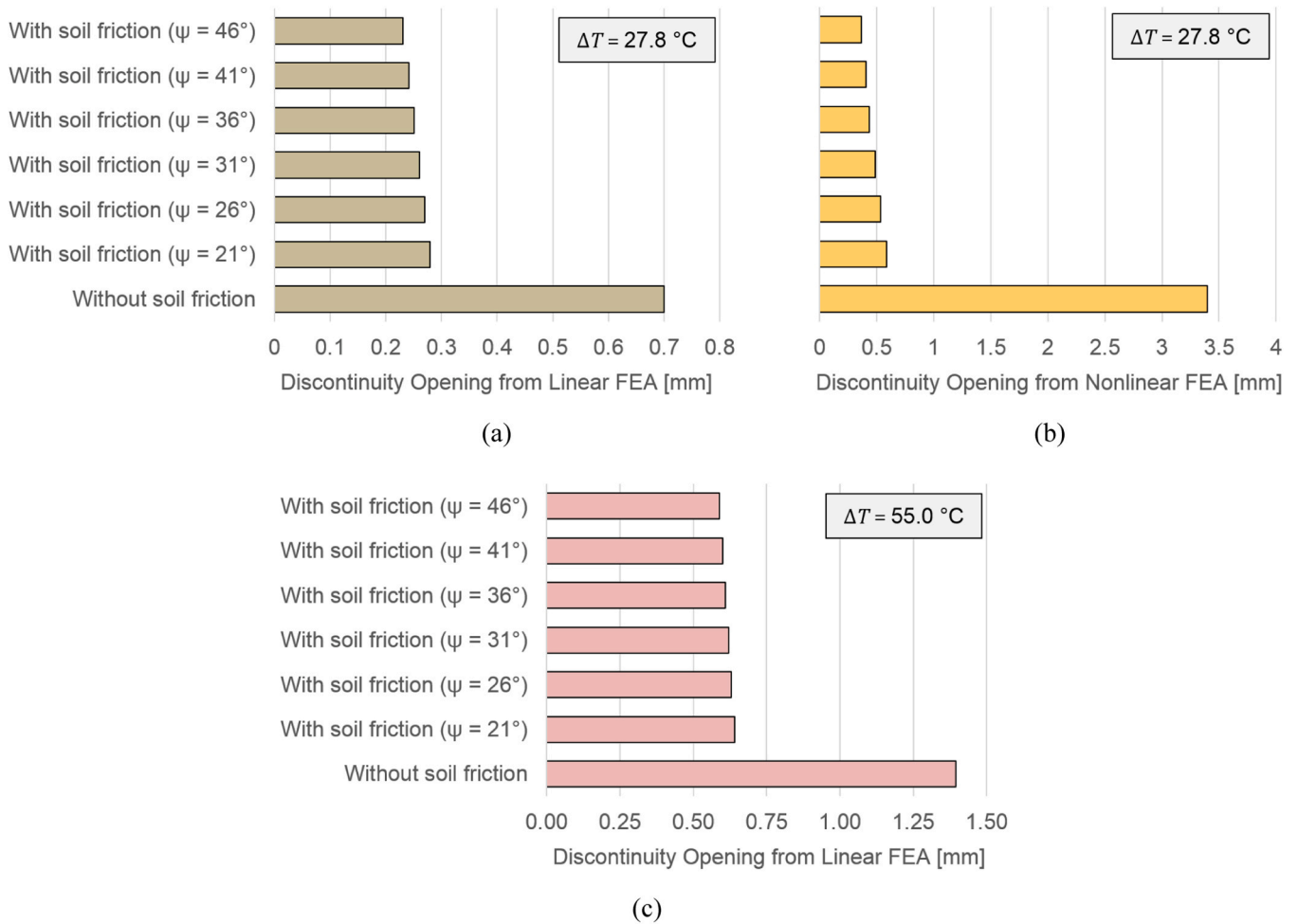
Fig. 27. Comparison of the obtained discontinuity opening values with and without the consideration of soil friction: (a) Linear FE analysis, $\Delta T = 27.8\,^{\circ}\text{C}$ (50 °F), (b) Nonlinear FE analysis, $\Delta T = 27.8\,^{\circ}\text{C}$ (50 °F), (c) Linear FE analysis, $\Delta T = 55.0\,^{\circ}\text{C}$ (99 °F).

follow the same trend. Comparison of Fig. 17a and b also shows that for a low value of the IRP's MoE, values of actual discontinuity opening calculated based on the upper, middle, and lower points along the host pipe thickness are close. However, as the IRP's MoE increases, the difference between these values grows larger. This implies that the values of ϕ_U, ϕ_M, and ϕ_L are close if the MoE of the IRP is small, and the difference between them grows larger as the MoE increases.

3.2.3. Parameters ϕ_U, ϕ_M, and ϕ_L: Role of geometry, material effects, and design formulation

3.2.3.1. Extreme values of ϕ_U, ϕ_M, and ϕ_L. The minimum and maximum values of ϕ_U, ϕ_M, and ϕ_L listed in Table 10 indicate that depending on the values of c, E_I, and t_I, large values may be obtained for these dimensionless parameters implying that there can be a quite big difference between the nominal discontinuity opening value obtained from Eqs. (16) and (17) and the actual discontinuity opening values along the thickness of the host pipe extracted from the FE analysis. The minimum values in Table 10 are corresponding to small values of the MoE and wall thickness of IRP. It can be seen that for a fixed value of the discontinuity width, minimum values of the parameters ϕ_U, ϕ_M, and ϕ_L are much closer to each other compared to the maximum values. This implies that for thin and low-modulus IRP materials, the change of the discontinuity opening along the thickness of the host pipe is far less significant compared to thick and high-modulus IRP materials. The maximum values in Table 10 were obtained from the models with large IRP's MoE and wall thickness. This means that as the thickness and/or MoE of IRP

increases, the deviation of the actual discontinuity openings from the corresponding nominal values predicted by Eqs. (16) and (17) becomes larger.

3.2.3.2. Effects of IRP's wall thickness and MoE on values of ϕ_U, ϕ_M, and ϕ_L. Fig. 18 depicts the effects of the wall thickness and MoE of IRP on values of parameters ϕ_U, ϕ_M, and ϕ_L for Type II discontinuity ($c = 12.7$ mm [1/2 in.]). Corresponding charts for Type I ($c = 6.35$ mm [1/4 in.]) and Type III ($c = 152.4$ mm [6 in.]) are not presented here for the sake of brevity. It can be clearly seen that the increase of both MoE and wall thickness of IRP results in the increase of ϕ_U, ϕ_M, and ϕ_L values. It can also be observed that for fixed values of E_I and t_I, the value of ϕ_U is always higher than ϕ_M, and the value of ϕ_M is always higher than ϕ_L.

Results also showed that in Types I and II discontinuities, for low values of the IRP's MoE, the change of parameters ϕ_U, ϕ_M, and ϕ_L with the IRP thickness follows a linear trend. However, as the MoE of IRP increases, this trend gradually tends to become nonlinear. Nonlinear change of the actual to nominal discontinuity opening ratio as a function of the IRP thickness is more highlighted in the parameter ϕ_U compared to parameters ϕ_M and ϕ_L. Such nonlinear trend was not observed for a large discontinuity width (Type III).

3.2.3.3. Effect of the IRP's thickness and MoE on variations of the ϕ along the host pipe thickness. Fig. 19 depicts the effects of the wall thickness and MoE of the IRP on variations of the actual to nominal discontinuity opening ratio (ϕ) along the thickness of the host pipe for Type II discontinuity ($c = 12.7$ mm [1/2 in.]. Corresponding charts for Types I

and III are not given for the sake of brevity. It can be seen that with the increase of the MoE of IRP, more significant changes are observed for the parameter ϕ along the thickness of the host pipe.

3.2.3.4. Effect of the discontinuity width on values of ϕ_U, ϕ_M, and ϕ_L.
Fig. 20 depicts the change of ϕ_U, ϕ_M, and ϕ_L with the IRP thickness for different values of the discontinuity width. It can be clearly seen that the increase of the discontinuity width leads to the decrease of ϕ_U, ϕ_M, and ϕ_L which means that as the discontinuity width decreases, the deviation of the actual discontinuity openings from the corresponding nominal values predicted by Eqs. (16) and (17) becomes larger.

3.2.3.5. Proposed equations for the calculation of ϕ_U, ϕ_M, and ϕ_L.
Based on 81 nonlinear regression analyses conducted on the FE results (Fig. 21), following equations are proposed for the calculation of dimensionless parameters ϕ_U, ϕ_M, and ϕ_L.

$$\phi_U = a_1\tau^2 + a_2\tau + a_3 \tag{49}$$

$$\phi_M = b_1\tau^2 + b_2\tau + b_3 \tag{50}$$

$$\phi_L = c_1\tau^2 + c_2\tau + c_3 \tag{51}$$

where the coefficients a_1 to c_3 can be calculated using the following equations (Fig. 22).

$$a_i = \vartheta_{Ui}e^2 + \xi_{Ui}e + \omega_{Ui} \quad ; \quad i = 1, 2, 3 \tag{52}$$

$$b_i = \vartheta_{Mi}e^2 + \xi_{Mi}e + \omega_{Mi} \quad ; \quad i = 1, 2, 3 \tag{53}$$

$$c_i = \vartheta_{Li}e^2 + \xi_{Li}e + \omega_{Li} \quad ; \quad i = 1, 2, 3 \tag{54}$$

In Eq. (49)—(54), parameters τ and e are defined as follows.

$$\tau = \frac{t_I}{t_H} \quad ; \quad e = \frac{E_I}{E_{I[\text{ref}]}} \quad ; \quad E_{I[\text{ref}]} = 10000 \text{ MPa} \tag{55}$$

Values of the coefficients ϑ_i, ξ_i, and ω_i to be used in Eq. (52)—(54) are summarized in Table 11 for Types I, II, and III discontinuities. Very high values obtained for the coefficients of determination ($R^2 > 0.98$) guaranty the accuracy of the fit (Figs. 21 and 22). The validity ranges for the applicability of Eq. (49)—(55) are $0.4 \leq \tau \leq 1.65$ and 1000 MPa (145.04 ksi) $\leq E_I \leq$ 69000 MPa (10007.6 ksi) covering a wide range of practical applications.

3.3. IRP's peak axial stress

3.3.1. Variations of nominal axial stresses with the soil properties and pipe's burial depth
Fig. 23 depicts the effects of the coefficient of lateral earth pressure at rest (K_0), friction angle between the soil and the host pipe (ψ), burial depth of the pipe (z), and effective unit weight of the soil (γ') on axial stress of the compound section and nominal axial stress of IRP in the discontinuity segment. It can be seen that the increase of all the four considered parameters results in the decrease of the compound section's axial stress as well as IRP's nominal axial stress. The reason is that the increase of these parameters leads to the increase of mobilized soil friction that results in the decrease of the pipe's total displacement (δ_T) and discontinuity opening due to the temperature change which consequently reduces the generated axial loads and stresses in the system.

3.3.2. The parameter η: Geometrical effects and design values
Fig. 24 demonstrates the change of the parameter η, defined in Eq. (29), with IRP's MoE and wall thickness. It can be clearly seen that the increase of the IRP's MoE generally leads to the increase of the η values (Fig. 24a). On the contrary, the increase of the IRP's wall thickness results in the decrease of η (Fig. 24b). As the discontinuity width decreases,

the η values go through larger variations due to the change of IRP's material and geometrical characteristics. For a large discontinuity width, η values tend to become more uniform getting closer to unity. This implies that for a large discontinuity width, average axial stress along the IRP thickness equals IRP's nominal axial stress predicted by the analytical solution (Eq. (28)). Based on FE results, the range of the parameter η was determined for the discontinuity types I, II, and III as given in Eq. (56).

$$0.82 \leq \eta_{\langle\text{Type I}\rangle} \leq 1.07$$

$$0.93 \leq \eta_{\langle\text{Type II}\rangle} \leq 1.00$$

$$0.99 \leq \eta_{\langle\text{Type III}\rangle} \leq 1.00 \tag{56}$$

3.3.3. Effects of geometrical parameters on SCFs and design formulation
Under any specific type of loading, the value of SCF, defined in Eq. (30), is independent from the magnitude of the applied load. The SCF value is mainly determined by the geometrical properties of the system and it is not a function of material properties [40]. Fig. 25a depicts the change of SCF values due to the change of the parameter τ and its interaction with the parameter ζ. These parameters are defined in Eq. (44). If the wall thickness of the host pipe is constant, the increase of τ results in the increase of the IRP thickness, and the increase of ζ leads to the increase of the discontinuity width.

It can be clearly observed in Fig. 25a that the increase of τ leads to the increase of the SCF value at the edge of a circumferential discontinuity in IRP systems. However, it should be noted that the amount of such increase is heavily influenced by the parameter ζ. As the value of ζ increases, from a Type I to a Type III discontinuity, the parameter τ becomes less effective on the SCF values. For $\zeta = 24$ (Type III discontinuity), the SCF is almost constant as the IRP thickness increases, while for $\zeta = 1$ (Type I discontinuity), the SCF value for $\tau = 1.65$ is over twice the corresponding value for $\tau = 0.4$. Fig. 25a also shows that for small values of τ, the increase of ζ leads to the increase of SCFs, while for large values of τ, the increase of ζ results in the decrease of the SCF values.

Based on nonlinear regression analyses conducted on the FE results (Fig. 25b—d), Eq. (57)—(59) are proposed for the calculation of SCFs in discontinuity types I, II, and III, respectively.

$$\text{SCF}_{\langle\text{Type I}\rangle} = -1.774\tau^3 + 5.4674\tau^2 - 3.7008\tau + 2.0304 \tag{57}$$

$$\text{SCF}_{\langle\text{Type II}\rangle} = 0.0177\tau^3 - 0.1303\tau^2 + 0.6417\tau + 1.3114 \tag{58}$$

$$\text{SCF}_{\langle\text{Type III}\rangle} = 0.0556\tau^3 - 0.2070\tau^2 + 0.2886\tau + 1.7281 \tag{59}$$

Very high values obtained for the coefficients of determination ($R^2 > 0.98$) for Eq. (57)—(59) guaranty the accuracy of the fit (Fig. 25b—d). The validity range for the applicability of Eq. (57)—(59) is $0.4 \leq \tau \leq 1.65$ which covers a wide range of practical applications.

3.4. Effects of material and geometric nonlinearities on the axial response

Values of input parameters for studying the effects of material and geometric nonlinearities on the discontinuity opening are listed in Table 12. Since according to Sects. 3.1 and 3.2.1, the most influential soil-related parameter on the axial response of the pipe subjected to the temperature change is the friction angle at the interface between the soil and the host pipe (ψ), this parameter has been selected as the main variable ($\psi = 21, 26, 31, 36, 41$, and $46°$) in the present section to study its effect on the discontinuity opening. Two levels of seasonal temperature changes were considered in the present research: $\Delta T = 27.8$ °C (50 °F) and 55.0 °C (99 °F). The reasons behind selecting these specific values have been discussed in Sect. 2.4.1. For the nonlinear analyses, ALTRA10® was selected as the IRP material; since it has been suggested as a solution for the rehabilitation of water pipelines [46] and its nonlinear stress-strain curve is available. A total of 72 linear and nonlinear FE analyses were conducted on generated models, and a

summary of results are shown in Fig. 26. Conducted FE analyses include 24 linear, 24 small-displacement nonlinear (material nonlinearity only), and 24 large-displacement nonlinear (both material and geometric nonlinearity) analyses.

Fig. 26 depict the change of actual discontinuity opening (δ_c) with the soil friction angle (ψ) for $\Delta T = 27.8\,°C$ (50 °F) and 55.0 °C (99 °F). It can be clearly seen that the increase of the soil friction angle results in the decrease of the discontinuity opening. It can also be seen that, depending on IRP's material behaviour, there might be a major difference between the results of linear and nonlinear analyses. According to Fig. 26a, for $\Delta T = 27.8\,°C$ (50 °F), the maximum discontinuity opening value obtained from the linear analysis is 0.280 mm, while the maximum values extracted from small-displacement and large-displacement nonlinear analyses are 0.585 mm (0.0230 in.) and 0.598 mm (0.0235 in.), respectively; which are over twice the corresponding outcome of the linear analysis. This finding highlights the importance of including the material nonlinearities in the FE analysis if the IRP material's behaviour may enter the nonlinear region subjected to seasonal temperature changes.

Fig. 26a indicates that for $\Delta T = 27.8\,°C$ (50 °F), results of small-displacement and large-displacement nonlinear analyses are almost the same. Hence, it can be concluded that if the maximum seasonal temperature changes of the pipelines in New York State and other parts of the Northeast US are of interest ($\Delta T = 27.8\,°C$ [50 °F]), geometric nonlinearity which makes the analysis computationally expensive do not need to be incorporated in the FE models. Fig. 26b shows that, for $\Delta T = 55.0\,°C$ (99 °F), the maximum discontinuity opening value obtained from the linear analysis is 0.640 mm (0.0252 in.), while the maximum values extracted from small-displacement nonlinear analysis is 3.271 mm (0.1288 in.), which is over five times the corresponding output of the linear analysis. It can also be seen that for $\Delta T = 55.0\,°C$ (99 °F), results of small-displacement and large-displacement nonlinear analyses can be different. For example, for $\psi = 46°$, actual discontinuity opening value obtained from the large-displacement nonlinear analysis is 17% larger than the corresponding value obtained from the small-displacement nonlinear analysis.

According to the true stress-strain curve of ALTRA10® extracted based on the information provided by CDCQ [45], fracture strain of ALTRA10® is 0.173 (Fig. 6b). Hence, if the discontinuity width is 12.7 mm (0.5 in.), the maximum discontinuity opening which can be sustained by ALTRA10® IRP before the failure is around $0.173 \times 12.7 = 2.2$ mm (0.0866 in.). This means that for $\Delta T = 55.0\,°C$ (99 °F) and $c = 12.7$ mm (0.5 in.), according to the results of nonlinear FE analysis, ALTRA10® IRP fails subjected to thermal stresses, while according to the results of linear FE analysis, ALTRA10® IRP is able to withstand such level of temperature change. This finding highlights the fact that where the material nonlinearities are significant, the results of linear analysis can be misleading. These results also indicate that a certain degree of unbonding can be beneficial for IRP systems as it helps the IRP material to better accommodate the thermal strains and associated stresses. Controlled unbonding is probably feasible in circumferential discontinuities at bell and spigot joints.

Fig. 26 also shows that the results of nonlinear analysis are much more affected by the soil friction angle compared to the outcomes of linear analysis. For $\Delta T = 27.8\,°C$ (50 °F), the maximum to minimum discontinuity opening ratio obtained from linear and nonlinear FE analyses are 1.21 and 1.60, respectively. For $\Delta T = 55.0\,°C$ (99 °F), this ratio is 1.09 and 1.28 for linear and nonlinear FE analyses, respectively. This means that the exclusion of material nonlinearities from the FE analysis might lead to an incorrect interpretation of the relative importance of various parameters affecting the system response.

Fig. 27 compares the discontinuity opening values obtained from linear and nonlinear FE analyses with and without the consideration of soil friction. No chart is provided for the results of nonlinear FE analysis at $\Delta T = 55.0\,°C$ (99 °F). The reason is that the discontinuity opening values in this case all lead to an axial strain which is beyond the fracture

strain of ALTRA10® and hence result in the failure of IRP. Fig. 27 shows that in both linear and nonlinear FE analyses, there is a significant difference between the discontinuity openings with and without the consideration of soil friction, which means that the inclusion of soil friction in the FE model is absolutely necessary in order to get realistic results for the response of the system subjected to temperature changes.

In order to assess the difference between the frictional and frictionless cases, the average value of discontinuity openings under different soil friction angles can be compared with the corresponding discontinuity opening value without the consideration of soil friction. According to Fig. 27a and b, at $\Delta T = 27.8\,°C$ (50 °F), the frictionless to frictional discontinuity opening ratio is 2.73 and 7.25 for linear and nonlinear FE analyses, respectively. This implies that the nonlinear response of the system is more affected by the inclusion of the soil friction compared to the corresponding linear response. Comparison of Fig. 27a and c indicates that as the value of ΔT increases from 27.8 °C (50 °F) to 55.0 °C (99 °F), the frictionless to frictional discontinuity opening ratio decreases from 2.73 to 2.27 implying that as the level of temperature change increases, soil friction becomes less effective in reducing the amount of discontinuity opening.

4. Conclusions

Structural responses of IRP systems subjected to seasonal temperature changes incorporating the effects of soil friction were investigated based on analytical and numerical approaches verified via experimental data and closed-form solutions. A total of 180 linear and nonlinear FE analyses were carried out to characterize the axial behaviour of IRP systems and investigate the effects of geometrical parameters and material properties as well as the internal pressure of the pipeline, burial depth of the pipe, and properties of the surrounding soil on the axial stresses and deformations of IRP systems with circumferential host-pipe discontinuities. A set of analytical expressions were developed to describe the loading and induced responses of a mechanical model for the IRP repair systems subjected to seasonal temperature changes. Afterwards, based on the FE results, five modification factors were derived and applied to the developed analytical expressions in order to obtain the peak axial stress of IRP and the opening of host-pipe circumferential discontinuity due to the temperature change incorporating the effects of soil friction. Key findings can be summarized as follows.

- The increases of the coefficient of lateral earth pressure at rest, friction angle between the soil and host pipe, effective unit weight of the soil, and burial depth of the pipe all result in the decrease of the required length for the mechanical model as well as the discontinuity opening and IRP's axial stress in the discontinuity segment. The reason is that the increase of these parameters leads to the increase of mobilized soil friction per unit length of the pipe which consequently results in the decrease of the pipe length required to neutralize the force induced by the temperature change and the decrease of the pipe's total displacement due to the temperature variation which eventually reduces the generated axial loads and stresses in the system.
- As the pipeline's internal pressure increases, a longer pipe should be considered in the mechanical model. With the increase of the maximum mobilized soil friction force per unit length (f_u), the internal pressure becomes less effective on mechanical model's pipe length. The increase of the pipe displacement required to mobilize the full soil resistance (δ_u) leads to the increase of the pipe length in an equivalent mechanical model. With the increase of f_u, the amount of δ_u becomes more effective on mechanical model's pipe length. The most effective soil-related parameter on the axial response of the system is the friction angle at the interface between the soil and the host pipe.
- There can be a quite big difference between the nominal and actual discontinuity opening values along the thickness of the host pipe. For

thin and low-modulus IRP materials, the variation of the discontinuity opening along the thickness of the host pipe is far less significant compared to thick and high-modulus IRP materials. With the increase of the IRP's thickness/MoE and decrease of the discontinuity width, the deviation of the actual discontinuity openings from the corresponding nominal values becomes larger.

- For large values of the IRP's MoE, the change of IRP thickness does not have a significant effect on the values of actual discontinuity opening obtained from the FE analysis. Such behaviour is not reflected in the nominal discontinuity opening values which consequently results in the increase of ϕ_U, ϕ_M, and ϕ_L values as the IRP thickness increases. On the contrary, for small values of the IRP's MoE, the decreases in nominal and actual discontinuity values due to the increase of IRP thickness follow the same trend.
- The increase of the IRP's MoE generally leads to the increase of the η values. On the contrary, the increase of the IRP's wall thickness results in the decrease of η. As the discontinuity width decreases, the η values go through larger variations due to the change of IRP's material and geometrical characteristics. For a large discontinuity width, η values tend to become more uniform getting closer to unity.
- The increase of τ leads to the increase of the SCF value at the edge of a circumferential discontinuity in IRP systems. The amount of such increase is heavily influenced by the parameter ζ. As the value of ζ increases, from a Type I to a Type III discontinuity, the parameter τ becomes less effective on the SCF values. For small values of τ, the increase of ζ leads to the increase of SCFs, while for large values of τ, the increase of ζ results in the decrease of the SCF values.
- Depending on IRP's material behaviour, there might be a major difference between the results of linear and nonlinear analyses. This finding highlights the importance of including the material nonlinearities in the FE analysis if the IRP material's behaviour may enter the nonlinear region subjected to seasonal temperature changes. Results of nonlinear analysis are much more affected by the soil friction angle compared to the outcomes of linear analysis, and the exclusion of material nonlinearities from the FE analysis might lead to over-/under-estimation of the relative importance of various parameters affecting the system's response.
- In both linear and nonlinear FE analyses, there is a significant difference between the discontinuity openings with and without the consideration of soil friction which means that the inclusion of soil friction in the FE model is absolutely necessary in order to get realistic results for the response of the system subjected to temperature changes. The nonlinear response of the system is more affected by the inclusion of the soil friction compared to the corresponding linear response, and as the level of temperature change increases, soil friction becomes less effective in reducing the amount of discontinuity opening.

The developed numerical and analytical models presented in this paper can reliably describe the linear and nonlinear axial behaviour of internal replacement pipe systems for host pipes with circumferential cracks. Depending on the pipe material, surrounding soil conditions, and stresses to which the pipeline is subjected, both circumferential and longitudinal cracks might happen. The study of longitudinal cracks retrofitted with IRP systems subjected to temperature change is proposed as a topic for future research works. Similarly, studying the radial stresses/deformations due to the temperature change is suggested as a potential subject for future research. When the temperature drops below the freezing point, the soil with moisture will freeze and expand, creating frost load. The frost load may apply considerable bending forces to the pipe. Investigating the behaviour of IRP systems subjected to frost loads fell outside the present research's scope and is proposed as another potential topic for future research works.

Declaration of Competing Interest

The authors declare no potential conflicts of interest with respect to the research, authorship, and/or publication of this article.

Acknowledgements

Appendix A. Derivation of the equivalent axial stiffness and CTE for the IRP-host pipe compound section

Consider the equivalent mechanical model of Fig. 2a with Segs. 2 and 3 removed. If the IRP and the host pipe are fully bonded, the total axial deformation (δ_T) of the pipe with a compound section, assuming the linear material behaviour, can be calculated as follows.

$$\delta_T = \frac{F_a}{k_T} = \frac{F_a}{k_I + k_H} \tag{A1.1}$$

where F_a is the tensile force that should be applied to the free end of the pipe with a compound section in order to obtain the same amount of axial deformation as if the system was directly subjected to temperature change; k_T is the total axial stiffness of the system; and k_I and k_H are the axial stiffnesses of the IRP and the host pipe, respectively.

$$k_I = \frac{E_I A_I}{l} \quad ; \quad k_H = \frac{E_H A_H}{l} \quad \rightarrow \quad k_I + k_H = \frac{E_I A_I + E_H A_H}{l} \quad \rightarrow \quad \delta_T = \frac{F_a l}{E_I A_I + E_H A_H} \tag{A1.2}$$

where l is the length of the pipe.

Comparison of Eq. (A1.2) with the general formula for the axial deformation (Fl/EA) leads to the following expression for the EA of the compound section.

$$E_C A_C = E_I A_I + E_H A_H \tag{A1.3}$$

The tensile force F_a can be obtained as follows.

$$F_a = F_I + F_H = \sigma_I A_I + \sigma_H A_H = E_I \varepsilon_I A_I + E_H \varepsilon_H A_H = E_I \alpha_I \Delta T A_I + E_H \alpha_H \Delta T A_H \quad \rightarrow \tag{A1.4}$$

$$F_a = (E_I \alpha_I A_I + E_H \alpha_H A_H) \Delta T \tag{A1.5}$$

Substitution of Eq. (A1.5) in Eq. (A1.2) leads to the following expression for the total axial deformation.

$$\delta_T = \frac{(E_I \alpha_I A_I + E_H \alpha_H A_H) l \Delta T}{E_I A_I + E_H A_H} \tag{A1.6}$$

Comparison of Eq. (A1.6) with the general formula for the axial deformation due to the temperature change ($\alpha l \Delta T$) leads to the following expression for the CTE of the compound section.

$$\alpha_C = \frac{E_I A_I \alpha_I + E_H A_H \alpha_H}{E_I A_I + E_H A_H} \tag{A1.7}$$

Appendix B. Derivation of the analytical expression for the transfer function μ

According to Eq. (16), the parameter μ is defined as follows.

$$\mu = \frac{(\delta_c)_n}{\delta_T} \tag{A2.1}$$

The $(\delta_c)_n / \delta_T$ ratio can be determined as follows (Fig. 2a).

$$\delta_T = \delta_{[Seg.1]} + \delta_{[Seg.2]} + \delta_{[Seg.3]} = \frac{F_T \left(\frac{L-c}{2}\right)}{E_H A_H + E_I A_I} + \frac{F_T c}{E_I A_I} + \frac{F_T \left(\frac{L-c}{2}\right)}{E_H A_H + E_I A_I} \quad \rightarrow \tag{A2.2}$$

$$\frac{(\delta_c)_n}{\delta_T} = \frac{\delta_{[Seg.2]}}{\delta_{[Seg.1]} + \delta_{[Seg.2]} + \delta_{[Seg.3]}} = \frac{\frac{F_T c}{E_I A_I}}{\frac{F_T(L-c)}{E_H A_H + E_I A_I} + \frac{F_T c}{E_I A_I}} = \frac{\frac{c}{E_I A_I}}{\frac{L-c}{E_H A_H + E_I A_I} + \frac{c}{E_I A_I}} \quad \rightarrow \tag{A2.3}$$

$$\frac{(\delta_c)_n}{\delta_T} = \frac{c}{E_I A_I \left(\frac{L-c}{E_H A_H + E_I A_I} + \frac{c}{E_I A_I}\right)} \tag{A2.4}$$

Appendix C. Derivation of the equations proposed for the calculation of pipe length (L)

Stewart et al. [35] equations have been revised in the present paper, as follows, to incorporate the effect of internal pressure in the calculation of pipe length (L). Parameter ΔT^* is the amount of the temperature change that is required to mobilize the full soil resistance; $\acute{l}$ is the amount of the pipe length that is required to mobilize the full soil resistance; and l is the amount of the pipe length that will generate enough friction force (F_f) to neutralize the forces induced by the temperature change (F_T) and the internal pressure (F_P).

When $|\Delta T|$ is higher than ΔT^*, the value of l should be larger than $\acute{l}$; and Eq. (22) can be derived as follows.

$$F_f = f_u(l - \acute{l}) + \frac{f_u \acute{l}}{2} \quad ; \quad F_T = \alpha_H |\Delta T| E_H A_H \quad ; \quad F_P = \sigma_l A_H = \nu \sigma_\theta A_H = \frac{\nu p_i D_{iH} A_H}{2 t_H} \tag{A3.1}$$

$$F_f = F_T + F_P \quad \rightarrow \quad f_u(l - \acute{l}) + \frac{f_u \acute{l}}{2} = \alpha_H |\Delta T| E_H A_H + \frac{\nu p_i D_{iH} A_H}{2 t_H} \tag{A3.2}$$

$$\rightarrow \quad f_u l - f_u \acute{l} + \frac{f_u \acute{l}}{2} = \alpha_H |\Delta T| E_H A_H + \frac{\nu p_i D_{iH} A_H}{2 t_H} \quad \rightarrow \quad f_u l = \alpha_H |\Delta T| E_H A_H + \frac{\nu p_i D_{iH} A_H}{2 t_H} + \frac{f_u \acute{l}}{2} \tag{A3.3}$$

$$\rightarrow \quad l = \frac{\alpha_H |\Delta T| E_H A_H}{f_u} + \frac{\nu p_i D_{iH} A_H}{2 f_u t_H} + \frac{\acute{l}}{2} \tag{A3.4}$$

When $|\Delta T|$ is lower than ΔT^*, the value of l should be smaller than $\acute{l}$; and can be derived as follows.

$$F_f = \frac{1}{2}\left(\frac{f_u}{\acute{l}}\right) l^2 \quad ; \quad F_T = \alpha_H |\Delta T| E_H A_H \quad ; \quad F_P = \frac{\nu p_i D_{iH} A_H}{2 t_H} \tag{A3.5}$$

$$F_f = F_T + F_P \quad \rightarrow \quad \frac{f_u l^2}{2 \acute{l}} = \alpha_H |\Delta T| E_H A_H + \frac{\nu p_i D_{iH} A_H}{2 t_H} \tag{A3.6}$$

$$\rightarrow \quad l^2 = \frac{2 \acute{l} \alpha_H |\Delta T| E_H A_H}{f_u} + \frac{2 \acute{l} \nu p_i D_{iH} A_H}{2 f_u t_H} \quad \rightarrow \quad l^2 = \frac{2 \acute{l} \alpha_H |\Delta T| E_H A_H}{f_u} + \frac{\acute{l} \nu p_i D_{iH} A_H}{f_u t_H} \tag{A3.7}$$

$$\rightarrow l = \sqrt{\frac{2 \acute{l} \alpha_H |\Delta T| E_H A_H}{f_u} + \frac{\acute{l} \nu p_i D_{iH} A_H}{f_u t_H}} \tag{A3.8}$$

References

[1] Shou KJ, Chen BC. Numerical analysis of the mechanical behaviors of pressurized underground pipelines rehabilitated by cured-in-place-pipe method. Tunn Undergr Space Technol 2018;71:544–54. https://doi.org/10.1016/j.tust.2017.11.005.

[2] Talebi M, Zeinoddini M, Elchalakani M, Asil Gharebaghi S, Jadidi P. Pseudo-random artificial corrosion morphologies for ultimate strength analysis of corroded steel tubulars. Structures 2022;40:902–19. https://doi.org/10.1016/j.istruc.2022.04.063.

[3] Cabral RMS, Ferreira ADM, Pimentel JT, Cabral MAF, Lyra PRM, Afonso SMB, et al. Assessment by finite element modeling of pipelines with corrosion defects based on River-Bottom Profile model. Eng Struct 2022;261:114246. https://doi.org/10.1016/j.engstruct.2022.114246.

[4] Zhang X, Fang H, Hu Q, Ma B, Hu S, Du M, et al. Mechanical performance of corroded reinforced concrete pipelines rehabilitated with sprayed-on cementitious liners subjected to combined loads. Tunn Undergr Space Technol 2022;120:104266. https://doi.org/10.1016/j.tust.2021.104266.

[5] Yan X, Wang X, Xiang W, Zhao Y, Ma B. Buckling behavior of Formed-in-Place-Pipe (FIPP) liners under groundwater pressure: an experimental investigation for buried municipal pipelines. Tunn Undergr Space Technol 2023;142:105397. https://doi.org/10.1016/j.tust.2023.105397.

[6] Dai J, Wang Z, Wang Z, Wang H, Ma J, Zhao Z. Shake table test and numerical analysis of the seismic response of buried long-distance pipeline under longitudinal non-uniform excitation. Structures 2023;47:1241–9. https://doi.org/10.1016/j.istruc.2022.11.133.

[7] Pan H, Li H, Li C. Seismic fragility analysis of free-spanning submarine pipelines incorporating soil spatial variability in soil-pipe interaction and offshore motion propagation. Eng Struct 2023;280:115639. https://doi.org/10.1016/j.engstruct.2023.115639.

[8] Zhang L, Zhao X, Yan X, Yang X. A new finite element model of buried steel pipelines crossing strike-slip faults considering equivalent boundary springs. Eng Struct 2016;123:30–44. https://doi.org/10.1016/j.engstruct.2016.05.042.

[9] Tsatsis A, Alvertos A, Gerolymos N. Fragility analysis of a pipeline under slope failure-induced displacements occurring parallel to its axis. Eng Struct 2022;262:114331. https://doi.org/10.1016/j.engstruct.2022.114331.

[10] Ariaratnam ST, El-Assaly A, Yang Y. Assessment of infrastructure inspection needs using logistic models. J Infrastruct Syst 2001;7(4):160–5. https://doi.org/10.1061/(ASCE)1076-0342(2001)7:4(160).

[11] Yang K, Xue B, Fang H, Du X, Li B, Chen J. Mechanical sensitivity analysis of pipe-liner composite structure under multi-field coupling. Structures 2021;29:484–93. https://doi.org/10.1016/j.istruc.2020.11.036.

[12] Najafi M, Gokhale S. Second Edition. Trenchless technology: Pipeline and utility design, construction, and renewal. US: McGraw-Hill Professional,; 2021.

[13] Lueke JS, Ariaratnam ST. Rehabilitation of Underground Infrastructure Utilizing Trenchless Pipe Replacement. Pract Period Struct Des Constr 2001;6(1). https://doi.org/10.1061/(ASCE)1084-0680(2001)6:1(25).

[14] Najafi M, Kim KO. Life-cycle-cost comparison of trenchless and conventional open-cut pipeline construction projects. Proc ASCE Pipeline Div Spec Congr (Pipeline Eng Constr) 2012:1–6. https://doi.org/10.1061/40745(146)61.

[15] Francom T, El Asmar M, Ariaratnam ST. Using alternative project delivery methods to enhance the cost performance of trenchless construction projects (Atlanta, Georgia, US.) Constr Res Congr, May 19–21 2014. https://doi.org/10.1061/9780784413517.125.

[16] Najafi M. Trenchless technology piping: Installation and inspection. US: McGraw-Hill Professional,; 2010. https://doi.org/10.1036/9780071640886.

[17] Gangavarapu BS, Najafi M, Salem O. Quantitative analysis and comparison of traffic disruption using open-cut and trenchless methods of pipe installation. Proc ASCE Int Conf Pipeline Eng Constr (N Pipeline Technol, Secur, Saf) 2012:1714–24. https://doi.org/10.1061/40690(2003)186.

[18] Kaushal V, Najafi M, Serajiantehrani R. Environmental impacts of conventional open-cut pipeline installation and trenchless technology methods: State-of-the-art review. J Pipeline Syst Eng Pract 2020;11(2):03120001. https://doi.org/10.1061/(ASCE)PS.1949-1204.0000459.

[19] Najafi M. Trenchless technology: Planning, equipment, and methods. US: McGraw-Hill Professional,; 2012. https://doi.org/10.1036/9780071762465.

[20] Saeed N, Kang W, Samali B. Composite overwrap repair of pipelines-reliability based design framework. Structures 2022;40:448–59. https://doi.org/10.1016/j.istruc.2022.04.029.

[21] Patnaik G, Rajput A. Safety assessment of underground steel pipelines with CFRP protection against subsurface blast loading. Structures 2023;54:1541–59. https://doi.org/10.1016/j.istruc.2023.06.001.

[22] Dixon PG, Tafsirojjaman T, Klingaman J, Hubler MH, Dashti S, O'Rourke TD, et al. State-of-the-art review of performance objectives for legacy gas pipelines with pipe-in-pipe rehabilitation technologies. J Pipeline Syst Eng Pract 2023;14(2):03122003. https://doi.org/10.1061/JPSEA2.PSENG-1371.

[23] Ha SK, Lee HK, Kang IS. Structural behavior and performance of water pipes rehabilitated with a fast-setting polyureaurethane lining. Tunn Undergr Space Technol 2016;52:192–201. https://doi.org/10.1016/j.tust.2015.12.003.

[24] Wang R, Wang F, Xu J, Zhong Y, Li S. Full-scale experimental study of the dynamic performance of buried drainage pipes under polymer grouting trenchless rehabilitation. Ocean Eng 2019;181:121–33. https://doi.org/10.1016/j.oceaneng.2019.04.009.

[25] Tafsirojjaman T, Manalo A, Tien CMT, Wham BP, Salah A, Kiriella S, et al. Analysis of failure modes in pipe-in-pipe repair systems for water and gas pipelines. Eng Fail Anal 2022;140:106510. https://doi.org/10.1016/j.engfailanal.2022.106510.

[26] Vasilikis D, Karamanos SA. Mechanical behavior and wrinkling of lined pipes. Int J Solids Struct 2012;49(23–24):3432–46. https://doi.org/10.1016/j.ijsolstr.2012.07.023.

[27] Argyrou C, Bouziou D, O'Rourke TD, Stewart HE. Retrofitting pipelines with cured-in-place linings for earthquake-induced ground deformations. Soil Dyn Earthq Eng 2018;115:156–68. https://doi.org/10.1016/j.soildyn.2018.07.015.

[28] Tien CMT, Manalo A, Dixon P, Tafsirojjaman T, Karunasena W, Flood WW, et al. Effects of the legacy pipe ends on the behaviour of pipe-in-pipe repair systems under internal pressure. Eng Fail Anal 2023;144:106957. https://doi.org/10.1016/j.engfailanal.2022.106957.

[29] Nuruddin M, DeCocker K, Sendesi SMT, Whelton AJ, Youngblood JP, Howarter JA. Influence of aggressive environmental aging on mechanical and thermo-mechanical properties of ultra violet (UV) cured in place pipe liners. J Compos Mater 2020;54(23):3365–79. https://doi.org/10.1177/0021998320913988.

[30] O'Rourke TD, Strait JE, Mottl N, Berger BA, Wham BP, Stewart HE, et al. Performance evaluation of aqua-pipe under earthquake-induced ground deformation. Final Report. Ithaca, NY, US: School of Civil and Environmental Engineering, Cornell University,; 2021.

[31] Adebola T, Moore I, Hoult N. Use of optical fibers to investigate strength limit states for pressure pipe liners spanning across circular perforations. J Pipeline Syst Eng Pract 2021;12(2):04021006. https://doi.org/10.1061/(ASCE)PS.1949-1204.0000523.

[32] PHMSA. CPF No. 5–2008-5016H: Notice of proposed corrective action order. Pipeline and Hazardous Materials Safety Administration, Lakewood, CO, US; 2019.

[33] Bing C., Kelly S. Cyber attack shuts down top U.S. fuel pipeline network. Reuters. Archived from the original on May 8, 2021.

[34] Jeon S, O'Rourke TD, Neravali AN. Repetitive loading effects on cast iron pipelines with cast-in-place pipe lining systems. J Transp Eng 2004;130(6):692–705. https://doi.org/10.1061/(ASCE)0733-947X(2004)130:6(692).

[35] Stewart HE, Weinberg SR, Berger BA, Strait JE. Slow cooling of cured-in-place liners for cast iron and steel gas pipelines. Final Report (Submitted to: NYSEARCH/Northeast Gas Association). Ithaca, NY, US: School of Civil and Environmental Engineering, Cornell University,; 2019.

[36] Dixon P.G., Salah A., Ahmadi H., Ulrich M.E., Hubler M.H., Dashti S., et al. An analytical approach for thermally induced axial deformation in rehabilitated pipelines. ASCE UESI Pipelines 2023 Conference, August 12–16, 2023; San Antonio, Texas, US. https://doi.org/10.1061/9780784485026.02.

[37] Bokaian A. Thermal expansion of pipe-in-pipe systems. Mar Struct 2004;17:475–500. https://doi.org/10.1016/j.marstruc.2004.12.002.

[38] Lu H, Wu X, Ni H, Azimi M, Yan X, Niu Y. Stress analysis of urban gas pipeline repaired by inserted hose lining method. Compos Part B: Eng 2020;183:107657. https://doi.org/10.1016/j.compositesb.2019.107657.

[39] ASCE. Guidelines for the seismic design of oil and gas pipeline systems. Committee on Gas and Liquid Fuel Lifelines. New York, US: American Society for Civil Engineering (ASCE),; 1984.

[40] American Petroleum Institute (A.P.I.). Recommended practice for planning, designing and constructing fixed offshore platforms-Working stress design: RP 2A-WSD. 21st Edition, US; 2007.

[41] Det Norske Veritas (DNV). Fatigue design of offshore steel structures, Recommended Practice: DNV RP C203. Norway; 2005.

[42] ANSYS. ANSYS mechanical APDL theory reference. Release 17.1, Canonsburg, US; 2016.

[43] Lee GH, Pouraria H, Seo JK, Paik JK. Burst strength behaviour of an aging subsea gas pipeline elbow in different external and internal corrosion-damaged positions. Int J Nav Archit Ocean Eng 2015;7(3):435–51. https://doi.org/10.1515/ijnaoe-2015-0031.

[44] Valves Instruments Plus (VIP) Ltd. Thermal expansion. UK: Valves Instruments Plus,; 2002.

[45] CDCQ. Characterization of 4 water main CIPP liner. Centre de développement des composites du Québec, Canada; 2021.

[46] Bureau M., Davison M., O'Rourke T.D. How bonded a bonded CIPP liner needs to be? A review of 3rd-party studies on CIPP KPI's. North American Society for Trenchless Technology (NASTT) 2021 No-Dig Show, March 28—April 1 2021; Orlando, FL, US.

[47] CDCQ. Characterization of coefficient of thermal expansion of water main CIPP material. Canada: Centre de développement des composites du Québec; 2022.

[48] Ahmadi H, Lotfollahi-Yaghin MA, Shao YB, Aminfar MH. Parametric study and formulation of outer-brace geometric stress concentration factors in internally ring-stiffened tubular KT-joints of offshore structures. Appl Ocean Res 2012;38:74–91. https://doi.org/10.1016/j.apor.2012.07.004.

[49] Ahmadi H, Lotfollahi-Yaghin MA, Shao YB. Chord-side SCF distribution of central brace in internally ring-stiffened tubular KT-joints: a geometrically parametric study. Thin-Walled Struct 2013;70(3):93–105. https://doi.org/10.1016/j.tws.2013.04.011.

[50] Ahmadi H, Lotfollahi-Yaghin MA, Asoodeh S. Degree of bending (DoB) in tubular K-joints of offshore structures subjected to in-plane bending (IPB) loads: Study of geometrical effects and parametric formulation. Ocean Eng 2015;102(7):105–16. https://doi.org/10.1016/j.oceaneng.2015.04.050.

[51] UK Health and Safety Executive. OTH 354: Stress concentration factors for simple tubular joints-assessment of existing and development of new parametric formulae. Prepared by Lloyd's Register of Shipping, UK; 1997.

[52] Hobbacher A.F. Recommendations for fatigue design of welded joints and components. IIW Document IIW-2259–15 ex XIII-2460–13/XV-1440–13, International Institute of Welding; 2016.

[53] Stewart H.E., O'Rourke T.D., Wham B.P., Netravali A.N., Argyrou C., Zeng X., et al. Performance testing of field-aged cured-in-place liners (CIPL) for cast iron

piping. Final Report (Submitted to: NYSEARCH/Northeast Gas Association), School of Civil and Environmental Engineering, Cornell University, Ithaca, NY, US; 2015.

[54] CIEST. External load testing of ALTRA10™ repaired specimens. Boulder, US: ARPA-E REPAIR Project Report, University of Colorado; 2022.

[55] Johnston VL. A study of elevated temperatures for natural gas piping in Arizona. Phoenix, Arizona, US: Arizona Corporation Commission; 1988.

[56] Meidani M, Meguid MA, Chouinard LE. Estimating earth loads on buried pipes under axial loading condition: insights from 3D discrete element analysis. Int J Geo-Eng 2018;9(5):1–20. https://doi.org/10.1186/s40703-018-0073-3.